Description and validation of the ice sheet model Nix v1.0

Daniel Moreno-Parada[1,2], Alexander Robinson[3,1], Marisa Montoya[1,2], and Jorge Alvarez-Solas[1,2]

[1]Departamento de Física de la Tierra y Astrofísica, Universidad Complutense de Madrid, Facultad de Ciencias Físicas, 28040 Madrid, Spain
[2]Instituto de Geociencias, Consejo Superior de Investigaciones Científicas-Universidad Complutense de Madrid, 28040 Madrid, Spain
[3]Alfred Wegener Institute, Helmholtz Centre for Polar and Marine Research, Potsdam, Germany

Correspondence: Daniel Moreno-Parada (danielm@ucm.es)

Abstract. We present a physical description of the ice-sheet model Nix v1.0, an open-source project intended for collaborative development. Nix is a 2D thermomechanical model written in C/C++ that simultaneously solves for the momentum balance equations, mass conservation and temperature evolution. Nix's velocity solver includes a hierarchy of Stokes approximations: Blatter-Pattyn, depth-integrated higher order, shallow-shelf and shallow-ice. The grounding-line position is explicitly solved by a moving coordinate system that avoids further interpolations. The model can be easily forced with any external boundary conditions, including those of stochastic nature. Nix has been verified for standard test problems. Here we show results for a number of benchmark tests from standard intercomparison projects and assess grounding-line migration with an overdeepened bed geometry. Lastly, we further exploit the thermomechanical coupling by designing a suite of experiments where the forcing is a physical variable, unlike previously idealised forcing scenarios where ice temperatures are implicitly fixed via an ice rate factor. Namely, we use atmospheric temperatures and oceanic temperature anomalies to assess model hysteresis behaviour with active thermodynamics. Our results show that hysteresis in an overdeepened bed geometry is similar for atmospheric and oceanic forcings. We find that not only the particular sub-shelf melting parametrisation determines the temperature anomaly at which the ice sheet retreats, but also the particular value of calibrated heat exchange velocities. Notably, the classical hysteresis loop is narrowed for both forcing scenarios (i.e., atmospheric and oceanic) if the ice sheet is thermomechanically active as a results of the internal feedback among ice temperature, stress balance and viscosity. In summary, Nix combines rapid computational capabilities with a Blatter-Pattyn stress balance fully coupled to a thermomechanical solver, not only validating against established benchmarks but also offering a powerful tool for advancing our insight on ice dynamics and grounding line stability.

1 Introduction

Marine ice sheets, such as the present-day West Antarctic Ice Sheet (WAIS), are of particular interest for the glaciological community and have been fundamental objects of study in the last decades (Shepherd et al., 2018; Rignot et al., 2019; Robel

et al., 2019; Pattyn and Morlighem, 2020). Since their bedrock lies mostly below sea level, they are subjected to rapid changes (Bentley, 1998), leading a number of authors to question their stability. A complete WAIS collapse would imply 5 to 6 metres

25 of level rise (Bentley, 1998; Fretwell et al., 2013), leaving the future of the WAIS as a key uncertainty for sea-level projections.

An accurate numerical description of the grounding line is thus fundamental for the reliability of such predictions. A number of attempts have been made in the past to simulate grounding-line migration within marine ice-sheet models. Weertman (1974) and Thomas and Bentley (1978) showed that no stable steady states of the grounding line could be found on inland-sloping or retrograde beds. Hindmarsh (1993) later introduced the possibility of neutral equilibrium under the premise that the equilibri-

30 ium position is continuous and hence there exists an infinite number of equilibrium configurations. More recently, Vieli and Payne (2005) assessed the influence of numerical details and discretization on the dynamics of the grounding line, concluding that a reliable method of treating grounding-line migration within numerical ice-sheet models was unknown. Later studies confirmed the possibility of numerical artefacts (Pattyn et al., 2006; Hindmarsh, 2006; Schoof, 2006a, b, 2011), in agreement with the early works of Weertman (1974) and Thomas and Bentley (1978). Even so, Vieli and Payne (2005) and Pattyn et al.

35 (2006) hypothesised the possibility of "neutral equilibrium", first introduced by Hindmarsh (1993). The analytical approach of Schoof (2007) based on assymptotic expansions eventually concluded that these results were numerical issues for certain parameter regimes. Only in the absence of basal sliding the possibility of non-unique steady states has been raised (Nowicki and Wingham, 2008).

Amidst the lack of a reliable model of grounding-line migration, the first Marine Ice Sheet Intercomparison Project (MISMIP,

40 Pattyn et al., 2012) shed light on the agreement of modelling efforts to describe the grounding line motion and assessed the appropriateness of numerical schemes. The authors proposed a set of benchmark experiments on an idealised two dimensional bed geometry, concluding that moving grid models are the most reliable choice from a numerical perspective as the grounding line is part of the solution and no interpolations are required.

MacAyeal and Barcilon (1988) notably showed that a two-dimensional free-floating shelf has no effect on the dynamics of

45 he grounded ice upstream of it (later underlined by Schoof, 2007). As a result, a boundary condition can be directly imposed at the grounding line that is solely dependent on the ice thickness therein, irrespective of the particular shape or the dynamics of the shelf. A correct description of a 2D marine ice sheet thus relies on an appropriate formulation of the grounded ice dynamics, specially near the terminus position where ice streaming is generally found.

For a comparison with the semi-analytical solutions of Schoof (2007), ice streaming (i.e., fast flowing ice due to basal

50 sliding) becomes a necessary condition given that the boundary layer theory assumes rapid sliding near the grounding line. Ice streams are in fact a distinct feature of ice sheets with no counterpart in other geophysical thin-film flows. These regions of rapidly flowing ice exhibit velocities even three orders of magnitude faster than the usual glacial ice, yet they only account for a small fraction of the total ice sheet area (e.g., less than 5% of the Antarctic ice sheet Bamber et al., 2000). Even so, it is important to represent them correctly to fairly evaluate ice outflow discharge, ice-sheet sensitivity and overall stability.

55 The rapid flow of ice streams fails to be explained by vertical shearing of ice. In other words, the friction at the bed is typically less than the driving stress predicted by a lubrication approximation (Whillans and van der Veen, 1997; Joughin et al., 2004). Rather, high ice stream velocities are caused by the deformation of meltwater-saturated, weak subglacial till (Alley

et al., 1986; Blankenship et al., 1986; Engelhardt et al., 1990). Thus consistent with geophysical studies showing that basal sliding is fundamentally a sort of Coulomb slip connected with the mechanical failure of plastic till (e.g., Tulaczyk, 1999).

60   Schoof (2006b) later extended the work to depth-integrated viscous flows used in three-dimensional ice-sheet models. Namely, a variational formulation of the two-dimensional Shallow Shelf Approximation (SSA) equations is given without assumptions on the extension of the sliding domain. In fact, as noted by the author, sliding regions must be determined as part of the solution and are consequently not known *a priori*. Notably, a solvability condition was also derived (as in Schoof, 2006b) to guarantee the existence of physical solutions. Strictly speaking, if the till is too weak so that the total momentum of applied

65   forces is greater than the maximum momentum of frictional force about a given point, then no solutions are expected to exist.

    A variational formulation entails strong consequences both from a physical and a mathematical point of view. Particularly, it eludes explicit manipulation of the unknown sliding domain extension, additionally provides a numerical method for solving the ice flow problem and it ensures well-posedness of the SSA non-linear elliptic equations since they can be derived from a convex and bounded below functional (Schoof, 2006b). However, the time-evolving system of the SSA stress balance coupled

70   to the advection equation is not yet known to be mathematically well posed (Bueler and Brown, 2009).

    More recently, Goldberg (2011) derived a higher-order stress approximation using variational methods with similar accuracy to the Blatter-Pattyn momentum equations (Blatter, 1995; Pattyn, 2003). The velocity solver was first adapted for multimillenial 3D ice-sheet models by CISM (Lipscomb et al., 2019), where this depth-integrated velocity approximation was referred to as DIVA. Nevertheless, the DIVA solver had been previously used in continental scale models by Arthern et al. (2015) and Arthern

75   and Williams (2017). The numerical stability of this solver was systematically studied by Robinson et al. (2022), where the authors show that the DIVA solver emerges as a clear outlier in terms of both model performance and its representation of the ice-flow physics itself.

    The appropriate stress balance treatment is merely one of the challenges of ice streaming and grounding line stability. Understanding the mechanisms governing its temporal variability also remains as a major obstacle particularly at the aim of

80   developing models of ice sheet dynamics (Robel et al., 2013). Given the broad range of ice flow speeds observed in real ice sheets (e.g., Shepherd and Wingham, 2007; Truffer and Fahnestock, 2007; Vaughan and Arthern, 2007), numerical simulations of these rapidly flowing bands are a well-known difficulty. Diverse approaches are found in the literature for varying dynamical complexity and basal hydrology.

    Despite the extensive research on the topic, important questions regarding the particular effect of thermodynamics remain

85   unanswered. Specifically, whether marine ice sheets have discrete steady surface profiles if ice temperatures can freely evolve in time and further the potential implications on the hysteresis behaviour in overdeepened bed geometries. In ice streaming regions, ice flow occurs mostly along one main direction, thus becoming the preferred axis across which lateral variations are negligible. It is a common approach to reduce the number of horizontal dimensions to the main flow direction so as to minimize computing time. Nonetheless, the thermal state of the ice and the potential oceanic forcing are still fundamental

90   pieces to understand the future evolution of ice sheets that have not been considered in low-dimensional models.

    We herein describe the 2D ice sheet model Nix. Unlike previous models, the default setup consists of a Blatter-Pattyn stress balance fully coupled to a thermodynamical solver that accounts for both vertical and along-flow horizontal heat advection, as

well as vertical diffusion. Note that other configurations are also possible given the independent structure of Nix funtionalities. In other words, the user can select a particular stress balance description from a hierarchy of Stokes approximations (i.e., Blatter-Pattyn, Depth Integrated Viscosity Approximation, SSA or SIA) and optionally solve the associated heat problem. The paper is structured as follows: we begin by describing the technical model design (Section 2). We then describe the physical approximations (Section 3) and numerics (Section 4) of the model. Several benchmarks and idealized experiments are presented in Section 5. A thorough discussion is given in Section 6 and the work is summarised in Section 7.

2 Model design

Nix is an open source software available under the Creative Commons Attribution 4.0 International license. The model has been derived from scratch with a clear Application Programming Interface (API). It is written in C/C++ for efficiency and extremely fast computing and is readily available to run in any High Performance Computing Cluster. There are two key dependencies: NetCDF and Eigen libraries. The former handles tasks for convenient community-standard input/output capability, whereas the latter serves to define vectors, matrices and further necessary computations (Fig. 1).

Nix's design offers a friendly Python wrapper module that handles directory management and compilation, though it can be compiled and run independently. The exact version used to produce the results of this work is archived at a persistent Zenodo repository (Moreno-Parada et al., 2023) while the latest version can be accessed on GitHub at: https://github.com/d-morenop/nix.

3 Model physics

In this section, the fundamental equations of the model are described. Generally speaking, we consider an ice slab of two spatial dimensions (i.e., horizontal and vertical) by coupling a particular choice of stress balance, the advection equation and the associated heat problem.

Our system is thought to thermodynamically evolve in time through three main processes: vertical difusion, horizontal and vertical advection and internal heat deformation of the ice. Viscosity is thus dependent on both the strain rate and the temperature. With respect to dynamics, basal friction can be parametrised by three distinct formulations (linear, power-law and Regularized-Coulomb). Additionally, the basal friction captures the thermal state of the base by a two-valued friction coefficient encapsulating frozen and thawed bedrocks.

3.1 The Blatter-Pattyn approximation

Ice sheets and glaciers are generally described as an incompressible fluid in a low Reynolds number flow. Conservation of momentum is then ensured if velocities satisfy the Stokes equations, a quasi-static stress description where intertial and advective terms are neglected due to the slow movement of the ice.
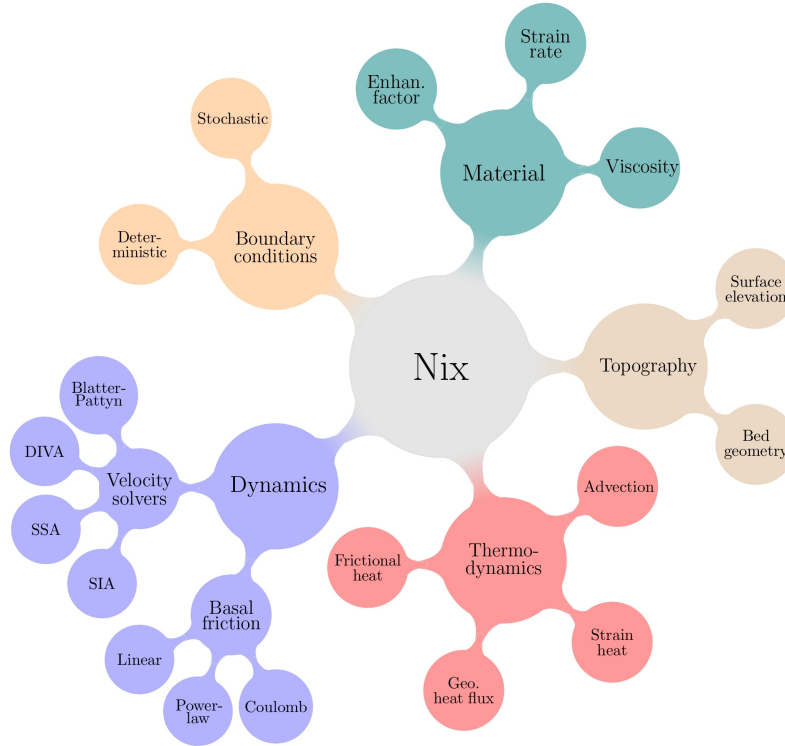
Figure 1. Overview of Nix modular structure. Each colour represents a C++ class: dynamics, material, topography, thermodynamics and boundary conditions. The Python wrapper is an optional user friendly option and the code can be compiled without any additional depedencies at any standard High Performance Computing Cluster.

The typical ice sheet geometry allows to further simplify the Stokes flow equations by the defining an aspect ratio ε. Given the characteristic length scales for the horizontal and vertical dimensions, $\varepsilon \ll 1$ (e.g., Greve and Blatter, 2009). Simply by keeping terms of order $\mathcal{O}(\varepsilon)$ in the Stokes equations, the Blatter-Pattyn model (Blatter, 1995; Pattyn, 2003) arises with a hydrostatic approximation error of $\mathcal{O}(\varepsilon^2)$ (Dukowicz et al., 2010; Schoof and Hindmarsh, 2010). This first-order approximation forms an elliptic coercive problem, significantly easier to solve than the intricate saddle-point problem of the full Stokes system.

For the purpose of this work, we shall consider two spatial dimensions: horizontal x and vertical z, respectively. This considerably reduces the computational time and allows for extremely high spatial resolutions, whilst explicitly accounting for the vertical gradients in ice viscosity and velocity. The 2D version of the Blatter-Pattyn model can be written as:

$$\frac{\partial}{\partial x}\left(4\eta\frac{\partial u}{\partial x}\right) + \frac{\partial}{\partial z}\left(\eta\frac{\partial u}{\partial z}\right) = \rho g \frac{\partial h}{\partial x}, \tag{1}$$

where ρ is the ice density, g is the gravitational acceleration, $\eta(x,z)$ is the effective viscosity, $h(x)$ is the surface elevation and $u(x,z)$ is the ice velocity.

The problem is subjected to a set of boundary conditions. Nix considers potential friction at the base of the ice, whereas a free surface on the upper boundary (Veen and Whillans, 1989). In terms of velocity gradients, the free surface condition can be expressed as (Pattyn, 2003):

$$\frac{\partial u}{\partial z} = 4\frac{\partial u}{\partial x}\frac{\partial h}{\partial x}, \tag{2}$$

and the basal drag is defined as the sum of all resistive forces:

$$\frac{\partial u}{\partial z} = 4\frac{\partial u}{\partial x}\frac{\partial b}{\partial x} + \frac{\tau(u)}{2\eta}, \tag{3}$$

for the base ($z = b$) in the presence of potential drag $\tau(u)$ (see Section 3.4 for a thorough description on basal friction). A stress-free base can be obtained simply by setting $\tau = 0$ in Eq. 3.

We further assume an ice divide at one end of the domain ($x = 0$), where $\partial u/\partial x = 0$ and hydrostatic equilibrium at the shelf-ocean boundary ($x = L$), where the water pressure balances the longitudinal stress gradient. The full problem thus takes the following succint form (subscripts hereinafter denotes partial differentiation):

$$\begin{cases} (4\eta u_x)_x + (\eta u_z)_z = \rho g h_x, & x \in \mathcal{I}, \ z \in \mathcal{L}, \\ u_z = 4u_x h_x, & x \in \mathcal{I}, \ z \in \partial\mathcal{L}^+, \\ 2\eta u_z = 8\eta u_x b_x + \tau, & x \in \mathcal{I}, \ z \in \partial\mathcal{L}^-, \\ u_x = 0, & x = 0, \ z \in \mathcal{L}, \\ 8\eta u_x = \rho g H^2 - \rho_w g z^2, & x = L, \ z \in \mathcal{L}, \end{cases} \tag{4}$$

where ρ_w is the water density, H is the ice thickness evaluated at the grounding line $x = L$ and the $\partial\mathcal{L}^\pm$ symbols denote the upper and lower vertical boundaries, respectively.

3.2 The Depth Integrated Viscosity Approximation

We now briefly describe the mathematical problem underlying the Depth Integrated Viscosity Approximation (DIVA) stress balance in Cartesian coordinates (Goldberg, 2011; Lipscomb et al., 2019).

As for the Blatter-Pattyn model, we shall consider only one horizontal dimension, leaving unaltered the nature of DIVA/SSA equations. This allows us to consider our model as a longitudinal section of a three-dimensional ice stream:

$$\frac{\partial}{\partial x}\left(4\bar{\eta}H\frac{\partial u}{\partial x}\right) + \tau(u) = \rho g H\frac{\partial h}{\partial x}, \tag{5}$$

Since the stress balance is also a second-order partial differential equation on the velocity, we again need two boundary conditions. Analogously to the Blatter-Pattyn approximation, we assume an ice divide at one end and, at the other end of the domain, the problem is subjected to a dynamic boundary condition that accounts for the balance between cryostatic and

hydrostatic pressures. Thus, we can express the DIVA/SSA boundary problem in the following compact form:

$$
\begin{cases}
(4\bar{\eta}Hu_x)_x + \tau(u) = \rho g H h_x, & x \in \mathcal{I}, \\
u = 0, & x = 0, \\
8\bar{\eta}u_x = \rho g H^2 - \rho_w g D^2, & x = L,
\end{cases}
\tag{6}
$$

where D is the distance from the sea surface to the bottom of the ice.

Equation 5 is an elliptic non-linear differential equation. In the purely SSA form (neither velocity nor viscosity dependency

160 on z, i.e., $u = \bar{u}$ and $\eta = \bar{\eta}$), it constitutes the simplest form of longitudinal stress balance derivable from the Stokes model (Bueler and Brown, 2009). We can then solve for the velocity $u(x)$ by integrating Eq. 6 if the functions $H(x)$, $\bar{\eta}(x)$, $h(x)$ and $\tau(u)$ are known. We have implemented an implicit algorithm so as to numerically integrate the one-dimensional DIVA/SSA equation (see integrating scheme description in Appendix A).

3.3 The advection coupling

165 Given that all models herein presented provide a quasi-static description of the ice flow, the stress balance does not determine the temporal evolution of the system, but rather it represents an equilibrium state for a particular ice thickness $H(x)$ and viscosity $\eta(x, z)$ configurations. The temporal evolution is generally considered by coupling the stress balance to the advection equation:

$$
H_t + (\bar{u}H)_x = S(x),
\tag{7}
$$

170 where $S(x)$ is the surface mass balance. Given that Eq. 7 is first order, we only need one boundary condition $H(x = 0, t)$ and the consequent initial condition $H(x, t = 0)$.

We now couple Eqs. 6 and 7 to study the evolution of the ice thickness $H(x, t)$ governed by the advection equation, where the velocity field $u(x, z)$ satisfies the stress balance imposed by a particular choice of the Stokes approximation. Namely, our problem takes the following mathematical form:

175
$$
\begin{cases}
H_t + (\bar{u}H)_x = S(x), & x \in \mathcal{I},\ t > 0 \\
(4\eta u_x)_x + (\eta u_z)_z = \rho g h_x, & x \in \mathcal{I},\ z \in \mathcal{L}, \\
H = H_0, & x \in \mathcal{I},\ t = 0. \\
h_x = 0, & x = 0,\ t > 0. \\
u = 0, & x = 0,\ t > 0. \\
8\eta u_x = \rho g H^2 - \rho_w g z^2, & x = L,\ z \in \mathcal{L},\ t > 0.
\end{cases}
\tag{8}
$$

From a purely physical perspective, Eq. 8 describes a fluid membrane of variable thickness driven by its own weight that evolves in time due to advection.

3.4 Basal friction

Basal shear stress can be generally expressed as a function of the sliding velocity u_b and the effective pressure N, i.e., $\tau_b =$
$f(u_b, N)$. The physical properties of the material over which the ice may potentially slide can correspond either to a hard
bedrock flow (e.g., Weertman, 1957) or to a Coulomb-plastic rheology (e.g., Tulaczyk et al., 1998). Moreover, the influence of
the sliding velocity on τ_b is often represented by a power friction law, although a regularization term u_0 accounting for local
properties of the bed has been shown to outperform such a power law in both pressurized ice experiments (Zoet and Iverson,
2020) and observations (Minchew et al., 2018; Stearns and van der Veen, 2018; Joughin et al., 2019)

As a result, Nix can calculate the basal shear stress (i.e., basal drag) via two independent formulations: a pseudo-plastic
power law (Schoof, 2010; Aschwanden et al., 2013) and the regularized-Coulomb law (Schoof, 2005; Joughin et al., 2019).
The former reads:

$$\boldsymbol{\tau}_b = -c_b \left(\frac{|\boldsymbol{u}_b|}{u_0} \right)^q \frac{\boldsymbol{u}_b}{|\boldsymbol{u}_b|}, \tag{9}$$

where $u_0 = 100$ m/yr and c_b is a spatially-variable friction coefficient defined below. We shall focus on two particular cases of
the pseudo-plastic law based upon the choice of the exponent q. Namely, the linear law ($q = 1$; e.g., Quiquet et al., 2018) and
the purely plastic law ($q = 0$).

On the other hand, the regularized-Coulomb formula is given by:

$$\boldsymbol{\tau}_b = -c_b \left(\frac{|\boldsymbol{u}_b|}{|\boldsymbol{u}_b| + u_0} \right)^q \frac{\boldsymbol{u}_b}{|\boldsymbol{u}_b|}, \tag{10}$$

behaving as a power law for small sliding velocities (i.e., $u_b < u_0$) whilst always yielding a bounded friction value for arbitrarily
high velocities (i.e., $u_b \gg u_0$). Following Zoet and Iverson (2020), we set $q = 1/5$ and $u_0 = 100$ m/yr by default to ensure a
reasonable transition to the steady-state shear stress supported by the till bed. The same study empirically established that q
remains unaffected by variations in the detailed bed surface geometry.

The basal drag coefficient β is usually defined as:

$$\beta = c_b(x)N, \tag{11}$$

where $N = \rho g H$ is the overburden pressure exerted by the ice column and $c_b(x)$ is a coefficient that reflects the bedrock
characteristics.

Nevertheless, for simplicity and consistency with prior benchmark experiments as MISMIP (Pattyn et al., 2012), the model
also allows to represent basal friction as:

$$\tau_b = C u^q, \tag{12}$$

with the chosen value of $C = 7.624 \times 10^6$ Pa m$^{-1/3}$ s$^{1/3}$ and $q = 1/3$, a sliding velocity of about 35 m yr^{-1} yields a basal
shear stress of 80 kPa.

3.5 Thermodynamics

The ice temperature in the flow line depends on the two spatial dimensions x and z (horizontal and vertical, respectively) along with time (i.e., $\theta = \theta(x, z, t)$). Heat transfer is further considered to occur due to vertical diffusion, both horizontal and vertical advection and internal heat deformation. Energy conservation is ensured in a classical approach by a balance equation (neglecting horizontal diffusion, Greve and Blatter, 2009):

$$
\begin{cases}
\rho c \theta_t = k \theta_{zz} - \rho c (u \theta_x + w \theta_z) + \Phi, & x \in \mathcal{I}, \ z \in \mathcal{L}, \ t > 0, \\
\theta = \theta_0, & x \in \mathcal{I}, \ z \in \mathcal{L}, \ t = 0, \\
\theta_z = -G/k, & x \in \mathcal{I}, \ z = \partial \mathcal{L}^-, \ t > 0, \\
\theta = \theta_L, & x \in \mathcal{I}, \ z = \partial \mathcal{L}^+, \ t > 0,
\end{cases}
\tag{13}
$$

where k is the ice conductivity, c is the specific heat capacity, $\Phi = 4 \eta \dot{\varepsilon}^2$ denotes the internal strain heating, G is the geothermal heat flow, θ_0 is the initial temperature profile and θ_L surface ice temperature. The $\partial \mathcal{L}^\pm$ symbols denote the upper and lower vertical boundaries, respectively.

The energy balance is discretised using an upwind scheme with a forward Euler step and centred differences for the spatial derivatives (see Appendix A4 for a detailed description).

3.6 Viscosity

We consider Glen's flow law (Glen 1955; Nye, 1957) to relate the shear stress, the ice temperature and the pressure of isotropic polycrystaline ice. Formation of anisotropic fabric is considered via a flow enhancement factor.

As shown in Section 3.1, the Blatter-Pattyn stress balance equations define the effective viscosity as:

$$
\eta = \frac{B}{2} \left(\dot{\varepsilon}^2 + \dot{\varepsilon}_0^2 \right)^{\frac{1-n}{2n}},
\tag{14}
$$

where B is the ice hardness, $n = 3$ is the exponent in Glen's flow law, $\dot{\varepsilon}^2$ is the effective strain rate and $\dot{\varepsilon}_0^2$ is a regularization factor to elude potential singularities when velocity gradients are zero. Notably, for a 2D model with explicit thermodynamics, the viscosity expression further simplifies the expression of B and $\dot{\varepsilon}^2$:

$$
B = A(\theta)^{-1/n},
\tag{15}
$$

$$
\dot{\varepsilon}^2 = \left(\frac{\partial u}{\partial x} \right)^2 + \frac{1}{4} \left(\frac{\partial u}{\partial z} \right)^2,
\tag{16}
$$

where $n = 3$ is the Glen-flow exponent. $A(\theta)$ is the rate factor and follows an Arrhenius law:

$$
A(\theta) = A_0 E e^{-Q/R\theta},
\tag{17}
$$

A_0 and Q are the temperature-dependent rate factor coefficient and activation energy, respectively (Greve and Blatter, 2009). E_f is the so-called enhancement factor, commonly used to approximate the effect of anisotropic flow. It is possible to specify

different values of the enhancement factor for different flow regimes (shear or stream). Typical values of the enhancement factor for the shearing and streaming regimes are $E_{\mathrm{shr}} = 3.0$ and $E_{\mathrm{strm}} = 0.7$ (Ma et al., 2010), respectively. Here we use for both a default value of $E = 1.0$.

For the vertically-integrated stress balance models (i.e., DIVA and SSA), Eqs. 14 and 15 are slightly modified by computing the vertically averaged quantities $\bar{\eta}$ and $\bar{B}$ following the generic formula $\bar{f} = \frac{1}{H} \int_b^h f \, dz$.

3.7 Grounding line

Nix aims at simulating the flow of a sliding ice sheet. The reason behind only explicitly modeling the grounded ice upstream of the grounding line lies on the fact that the longitudinal stress at $x = L$ is simply a function of the ice thickness $H(x = L)$ (Schoof, 2007) and therefore, the behaviour of grounded ice and the location of the grounding line itself are completely independent of the floating part, since the model only considers one horizontal dimension.

Neither the potential distinct shapes of the ice shelf (e.g., due to sub-shelf melting) nor the calving affect the dynamics of grounded ice. Thus, the flotation condition and the stress condition (Eq. 8) can be considered as boundary conditions at the grounding line. These two conditions are in fact sufficient to study the ice thickness evolution and the grounding-line migration.

Following Hindmarsh (1996), an explicit expression for the grounding-line migration rate $\dot{L}$ can be readily obtained from a total differentiation of the flotation condition:

$$\dot{L} \equiv \frac{dL}{dt} = \frac{\varrho D_t + (\bar{u}H)_x - S}{H_x - \varrho D_x},$$

(18)

where D is the water depth at the grounding line and $\varrho = \rho_w / \rho$ is the water-to-ice density ratio, respectively.

More recent studies suggest that the maximum terminus thickness is bounded by the yield strength of ice τ_c (Bassis and Walker, 2012; Bassis and Jacobs, 2013). Hence, a maximum ice thickness at the terminus occurs when the stress exceeds the depth integrated strength of ice:

$$H^{\mathrm{max}} = \frac{\tau_c}{\rho g} + \sqrt{\left(\frac{\tau_c}{\rho g}\right)^2 + \frac{\rho_w}{\rho} D^2},$$

(19)

thus constraining the terminus thickness such that $H(x = L, t) \leq H^{\mathrm{max}}$.

This approach eludes semi-empirical parametrizations of the calving (as in Schoof, 2007) and further provides a lower bound on the rate of grounding line advance (Bassis et al, 2017). Combining the continuity equation and the material derivative of H^{max} (Eq. 19), an expression for the rate of advance/retreat of the terminus can be readily obtained:

$$\frac{dL}{dt} \geq \frac{H_t}{H_x^{\mathrm{max}} - H_x},$$

(20)

at $x = L$. Negative sign indicates retreat.

Inequality Eq. 20 is analogous to the grounding-line migration derived for a marine ice sheet by Schoof (2007a; 2007b). Particularly, if H^{max} is given by the flotation condition, Eq. 20 exactly reproduces the grounding line position derived by Schoof (2007b) (Bassis et al., 2017).

3.8 Sub-shelf melting parametrization

Oceanic melting beneath ice shelves is the main driver of the current mass loss of the Antarctic ice sheet. For this reason, Nix considers various melting parameterisations from simple scalings with far-field thermal driving (e.g., Favier et al., 2019).

265 We adhere to local yet physically-based parametrizations based on a more complex ocean circulation models (Grosfeld et al., 1997). Namely, the linear dependency can be expressed as:

$$M = \gamma_T \frac{\rho_\mathrm{w} c_\mathrm{po}}{\rho L_\mathrm{i}} \left(T - T_0\right), \tag{21}$$

where γ_T is the heat exchange velocity, T_0 is a reference temperature, c_po the specific heat capacity of the ocean mix layer and L_i the latent heat of fusion of ice.

270 This linear formulation with a constant exchange velocity γ_T assumes a circulation in the ice-shelf cavity that is independent from the ocean temperature. This assumption is neither supported by modelling (Holland et al., 2008; Donat-Magnin et al., 2017) nor by observational studies (Jenkins et al., 2018) that suggest a larger circulation in response to a warmer ocean, subsequently increasing melt rates. One manner to account for this positive feedback is by considering a quadratic dependency (Holland et al., 2008):

275 $$M = \gamma_T \left(\frac{\rho_\mathrm{w} c_\mathrm{po}}{\rho L_\mathrm{i}}\right)^2 \left(T - T_0\right)^2. \tag{22}$$

These two parametrization have been employed in numerous studies (e.g., review in Asay-Davis et al., 2017; Favier et al., 2019). By default, Nix uses this quadratic parametrization.

4 Model numerics

4.1 Moving grid transformation

280 Nix uses a nonuniform moving spatial grid that explicitly solves the grounding line position. By default, the grid points distribution yields higher resolution near the grounding line following a polynomial or an exponential law. Evenly-spaced grids are also possible by setting the polynomial order to one.

As already noted by Pattyn et al. (2012), moving grid models are presumably the best choice from a numerical perspective, as the grounding line position $L(t)$ is part of the solution and no interpolations are further required. Given that neither the

285 terminus position $L(t)$ (i.e., the grounding line) nor the ice thickness $H(x,t)$ are fixed in time, we adopt a moving grid to trace their positions:

$$\sigma = \frac{x}{L(t)}, \ \ \zeta = \frac{z - b(x)}{H(x,t)}, \ \ \tau = t, \tag{23}$$

thus mapping the time-dependent intervals $0 \leq x \leq L(t)$ and $0 \leq z \leq H(x,t)$ into fixed ones $0 \leq \sigma \leq 1$ and $0 \leq \zeta \leq 1$. The variable τ is merely introduced to distinguish partial derivatives defined holding both σ and ζ constant (as opposed to hold x

290 and z constant).
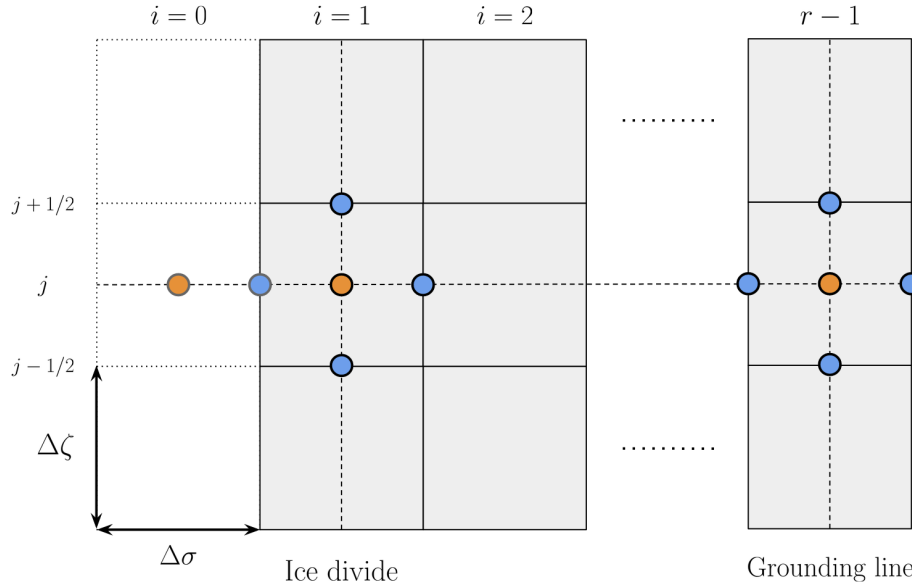
Figure 2. Nix staggered grid definition follows an Arakawa-C scheme (Arakawa and Lamb, 1977). The number of grid points the the horizontal r and vertical p is fixed in time (see Appendix A). As we employ a moving grid, the position of the last horizontal point $(r - 1/2)$ explicitly tracks the grounding line $L(t)$. The grid spacing in the vertical $\Delta\zeta_j$ and horizontal $\Delta\sigma_i$ axis can be spatially dependent as Nix allows for nonuniform grids. Ghost points required to satisfy the boundary condition at the ice divide are noted in grey edge colour.

As a result, the corresponding derivatives contain additional terms (directly applying the Leibniz rule):

$$\frac{\partial}{\partial z} = \frac{1}{H}\frac{\partial}{\partial \zeta}, \tag{24}$$

$$\frac{\partial}{\partial x} = \frac{1}{L}\frac{\partial}{\partial \sigma} - \frac{1}{H}\left[(1-\zeta)\frac{\partial b}{\partial \sigma} + \zeta\frac{\partial H}{\partial \sigma}\right]\frac{\partial}{\partial \zeta}, \tag{25}$$

$$\frac{\partial}{\partial t} = \frac{\partial}{\partial \tau} - \frac{\sigma}{L}\frac{\partial L}{\partial \tau}\frac{\partial}{\partial \sigma} - \frac{\zeta}{H}\frac{\partial H}{\partial \tau}\frac{\partial}{\partial \zeta}. \tag{26}$$

295   For simplicity and analogously for the Blatter-Pattyn approximation, the advection equation coupled with the SSA/DIVA stress balance can be written in terms of the new variables. Thus, Eq. 8 reads:

$$\begin{cases} LH_\tau - \sigma\dot{L}H_\sigma + (uH)_\sigma = LS(\sigma,\tau), & \sigma \in \tilde{\mathcal{I}}, \; \tau > 0 \\ (4\bar{\eta}Hu_\sigma)_\sigma + \tau L^2 = L^2\rho g h_\sigma & \sigma \in \tilde{\mathcal{I}}. \\ H = H_0, & \sigma \in \tilde{\mathcal{I}}, \; \tau = 0. \\ H_\sigma = 0, & \sigma = 0, \; \tau > 0. \\ u = 0, & \sigma = 0, \\ 4\eta u_\sigma = \left(\rho g H^2 - \rho_w g D^2\right) L/2, & \sigma = 1, \end{cases} \tag{27}$$

where $\tilde{\mathcal{I}} \in [0,1]$ is the transformed interval and the subscripts denote partial differentiation.

Likewise, the third evolution equation that determines the behaviour of our system (i.e., the energy balance, Eq. 13) can be
300   readily obtained in terms of our new variables:

$$
\begin{cases}
\rho c \left[L\theta_\tau - \sigma \dot{L}\theta_\sigma - \zeta L H_\tau \theta_\zeta / H \right] = \\
\quad kL\theta_{\zeta\zeta}/H^2 - \rho c u \left[\theta_\sigma - (b_\sigma + \zeta H_\sigma)\theta_\zeta / H \right] + L\Phi, & \sigma \in \tilde{\mathcal{I}},\ \zeta \in \tilde{\mathcal{L}},\ \tau > 0, \\
\theta = \theta_0, & \sigma \in \tilde{\mathcal{I}},\ \zeta \in \tilde{\mathcal{L}},\ \tau = 0, \\
\theta_z = -G/k, & \sigma \in \tilde{\mathcal{I}},\ \zeta = \partial \tilde{\mathcal{L}}^-,\ \tau > 0, \\
\theta = \theta_L, & \sigma \in \tilde{\mathcal{I}},\ \zeta = \partial \tilde{\mathcal{L}}^+,\ \tau > 0,
\end{cases}
\tag{28}
$$

where the transformed intervals are again denoted by $\tilde{\mathcal{I}}$ and $\tilde{\mathcal{L}}$ respectively.

4.2   Spatial integration

4.2.1   Implicit scheme and Picard iteration

305   The lateral boundary condition is in fact non-trivial to implement using an explicit scheme (e.g., a shooting-like method)
since it depends on the first spatial derivative of the velocity at the terminus position $\sigma = 1$, which might lead to convergence
issues. Nix thus includes an alternative velocity solver based on an implicit discretization shcheme of all stress balance models
described in Section 3 (numerical details in Appendix 3).

To account for the potential non-linearity in the velocity as a consequence of the viscosity and basal friction $\tau(u)$, the implicit
310   solver uses a initial guess τ_0 and η_0 and then enters a Picard iteration (see Theorem 2.2 in Teschl, 2012). A solution is hence
obtained when the convergence criterion:

$$
\frac{||u^n - u^{n-1}||}{||u^n||} < \phi_{\text{tol}}
\tag{29}
$$

is satisfied. The tolerance ϕ_{tol} can be set by the user but the default value is 10^{-6}.

For the Blatter-Pattyn approximation, a sparse matrix must be solved in each Picard iteration. To do so, we apply a Bi-
315   conjugate Gradient Stabilized method (commonly known as BiCGSTAB) with an Incomplete preconditioner (ILUT). On the
contrary, the DIVA/SSA approximation solely requires solving a tridiagonal matrix at in each Picard iteration step, where the
ice viscosity is updated. A tridiagonal solver algorithm is implemented as a subroutine within Nix to avoid additional external
dependencies (see Appendix A).

4.3   Time integration

320   Once the velocity field $u(x,z)$ is obtained for a given set of boundary conditions and a particular ice thickness initial distribution
$H(\sigma, \tau_0)$, we can compute the time evolution of the latter as a consequence of the advection imposed by $\bar{u}(x)$ and the surface
mass balance $S(x,t)$ (Eq. 7). Thus, this coupled system formed by the momentum conservation and the continuity equation
(Eq. 27) is fully integrated in two steps: first, a spatial integration to obtain the velocity velocity (where the ice viscosity

is known); and then, a forward time integration to determine the new ice thickness. Lastly, the energy balance equation is
325 integrated to compute the new temperature field.

Specifically, for a given initial ice thickness distribution $H(x, t_0)$, the stress balance equation is spatially integrated, thus
yielding the velocity $u(x, z)$. Then, the solution $u(x, z)$ (at t_0) and $H(x, t_0)$ allow us to integrate the continuity equation
forward in time, consequently obtaining $H(x, t_0 + \Delta t)$. Additionally, this new ice thickness distribution yields $\theta(x, z, t_0 + \Delta t)$,
thus constituting a self-consistent iterative method.

5 Methods and experimental set-up

Prior to any comprehensive description of the results, we must test whether Nix is capable of reproducing the benchmark tests
of the "Marine Ice Sheet Model Intercomparison Project" (MISMIP, Pattyn et al., 2012). We will perform all three MISMIP
experiments: relaxation to steady state on a downward-sloping bed (Exp. 1), reversal of parameter changes (Exp. 2) and
hysteresis on an overdeepening bed (Exp. 3). The aim of Exp. 1 was to show that there should be a single stable equilibrium
335 profile on a downward-sloping bed. A backwards parameter relaxation in Exp. 2 was thought to demonstrate that grounding
line positions should be identical during advance and retreat, as steady states are unique. Exp. 3 was then built to assess whether
ice sheet models exhibit hysteresis behaviour and has become a benchmark for testing the capability of numerical models to
simulate grounding-line migration

First, we adopt the exact same problem definition so as to perform a one-to-one comparison. Next, we run an ensemble of
340 simulations to address the question of whether the hysteresis with respect to model parameters variations found in in MISMIP
Exp. 3 is still present even if the thermal state of the ice can evolve in time (as opposed to the idealised constant ice factor
set in Pattyn et al., 2012). Fixing a value of the ice factor A uniquely determines a constant ice temperature, since $A(T')$ is
a bijective function of the temperature. We therefore impose an atmospheric forcing (i.e., the ice surface boundary condition)
that spans a wide range of realistic temperatures. As the geothermal heat flux provides a positive energy contribution, we
345 expect a different thermal equilibrium profile for each imposed surface temperature. This yields a different viscosity field for
each scenario, consequently leading to a different equilibrium velocity. As noted by Sergienko et al. (2013), the temperature
profile is mostly determined by horizontal advection in streaming regions, thus bringing forward a strongly non-linear feedback
worthy of attention.

Lastly, we force the system via ocean temperature anomalies with respect to a reference value T_0, so that $\Delta T_{\text{oce}} = T_{\text{oce}} - T_0$,
350 whilst holding constant the air temperature throughout the simulation. We then convert these temperature anomalies into sub-
shelf melting at the grounding line (e.g., Favier et al., 2019) by computing any of the parametrizations shown in Section 3.8.
Even though the air temperature is held constant (i.e., the boundary condition of our heat problem), the thermal state of the
ice may evolve as both the thickness and extent are perturbed by the changing sub-shelf melting at the grounding line. Our
particular ocean forcing consist of steps of 0.5ºC evenly-spaced in time by 30 kyr to ensure equilibration, from $\Delta T_{\text{oce}} = 0$ to a
355 maximum applied anomaly of 7ºC. Then, we reverse the forcing to recover the unperturbed state (i.e., zero anomaly).

It is worth noting that the basal friction remains identical to MISMIP experiments both for the atmospheric and oceanic forcings. This means that no additional dependency of friction on temperature or hydrology is considered.

Table 1. Nix suite of experiments. The first row replicates MISMIP benchmark tests, whereas MISMIP-therm explores the hysteresis behaviour of a thermomechanically active ice sheet in two different forcing scenarios: amospheric and oceanic.

Experiment name	Forcing variable	Thermodynamics	Melting/calving at GL
MISMIP (Exp. 1, 2 and 3)	Ice rate factor A	No	No
	Air temperature T_{air}	Yes	No
MISMIP+therm (Exp. 3)		No ($A = $ const.)	Yes
	Ocean temperatures anom. ΔT_{oce}	Yes ($A = f(T)$)	Yes

6 Results

6.1 MISMIP benchmark experiments

360 As a performance test for our flowline model, we have replicated the three main MISMIP experiments shown in Pattyn et al. (2012). In general, results obtained (Fig. 3) reproduce the results shown for models that employ a stretched coordinate system as ours.

We find no stable equilbirum states for the upward-sloping bed of Exp. 3 (Fig. 3c and 3c), in agreement with the theoretical considerations by Weertman (1974) and Schoof (2007). Namely, as we gradually decrease A (i.e., increasing ice viscosity),

365 the grounding line postition advances accross a downward sloping bed until the upward-sloping region is reached (Fig. 3c). The ice flux at the grounding line then continuous to increase due to the A forcing applied. Illustrated by Fig. 3d, when the ice flux is large enough so that there exists a stable solution beyond the unstable region (at the right-hand side of the bedrock local maximum in Fig. 3c), the grounding line traverses the upwards-sloping sector reaching the new stable solution.

Additionally, we repeat the three MISMIP experiments using the more sophisticated velocity solvers available in Nix: DIVA

370 and Blatter-Pattyn. A direct inspection of Figs. 3b and 3d reveals that the solutions are nearly identical to the simpler SSA version, both for a downwards sloping and the overdeepending beds. The hysteresis is particularly well captured in all three Stokes approximations and thus we will use the SSA solver in the remainder of the current work to minimise computational costs unless otherwise stated.

6.2 MISMIP + thermodynamics

375 To exploit the fact that Nix is fully coupled with a thermodynamic solver, we further investigate the equilibrium states (Schoof, 2007) when the system is forced via two scenarios: air temperatures T_{air} and ocean temperature anomalies ΔT_{oce}. Both describe a more realistic scenario with slight variations. The former implies the same underlying perturbation mechanism (compared to the idealised rate factor A forcing): temperature changes within the ice modify its viscosity so that the grounding
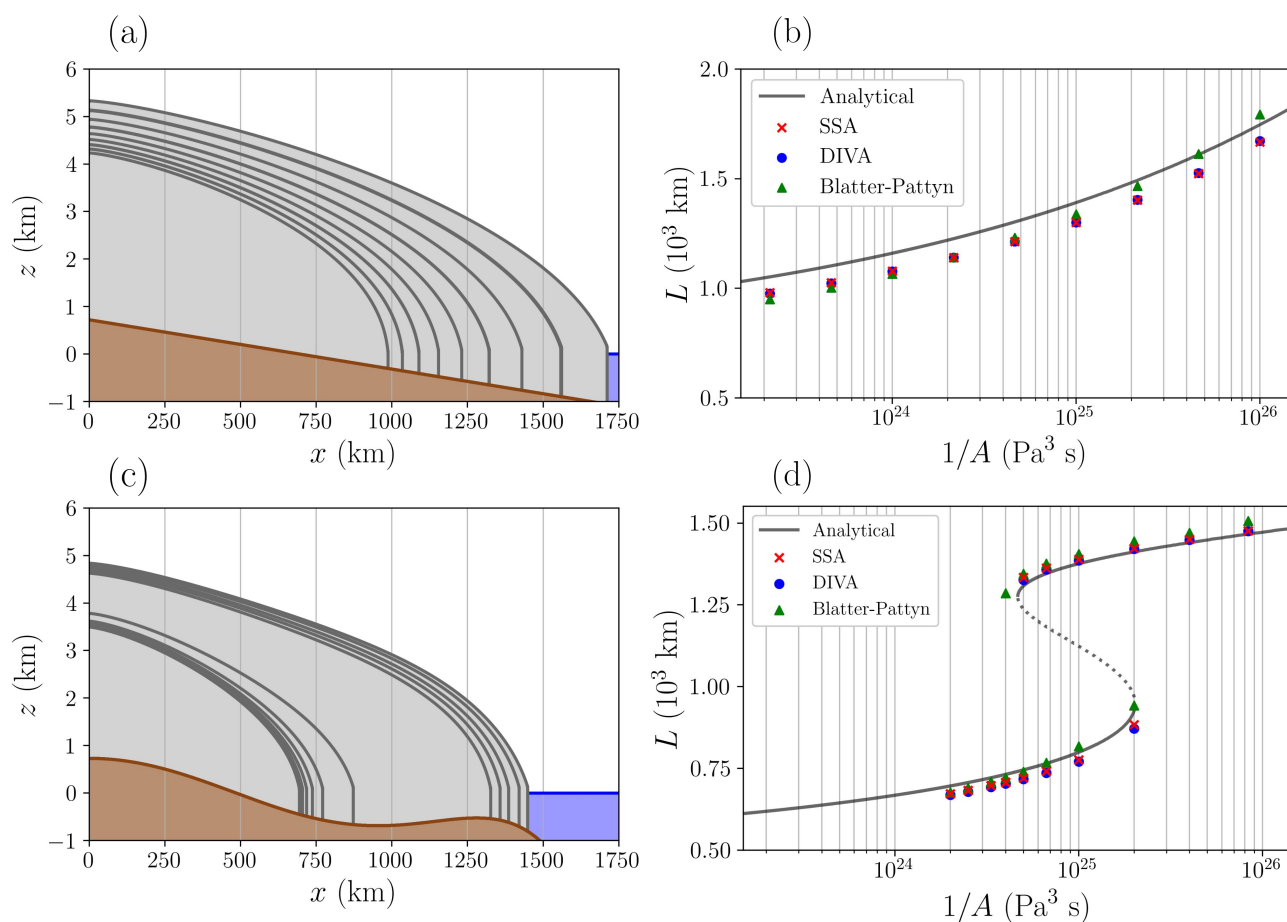
Figure 3. Left column: ice sheet extent. Right column: grounding-line position as a function of the MISMIP forcing A for three independent Stokes approximations: SSA, DIVA and Blatter-Pattyn. Grey line represents the analytical solution at equilibrium from Schoof (2007): solid line, stable branch; dashed line, unstable. Markers represent Nix results after the equilibration time given in Pattyn et al. (2012). Bed geometries correspond to Experiments 1 and 2 (first row) and Experiment 3 (second row), respectively.

line migrates to reach a new equilibrium position. Nevertheless, when forcing the system with ocean temperature anomalies
380 ΔT_{oce} while keeping the air temperature constant, we perturb the system via an ice flux at the grounding line. By separately studying each mechanism, we can determine whether a marine terminating ice sheet might undergo hysteresis in different scenarios.

6.2.1 Air temperature T_{air} forcing

At the aim of building a thermomechanically active version of MISMIP experiments, the natural choice is to convert the
385 idealised ice rate factor forcing in MISMIP into temperatures (via an Arrhenius law, Eq. 17) and use it explicitly as a forcing of the new experimental setup. Nevertheless, the corresponding temperature range (see grey shading in Fig. 4a) does not yield a full advance or retreat of the ice sheet.

This significantly reduced grounding line migration is a consequence of our active thermal evolution of the ice. For a given air temperature value T_{air}, the geothermal heat flux and basal frictional heat ensure that the lower half of the ice sheet
390 remains warmer, thus leading to an overall less viscous ice sheet than the corresponding value of $A(T_{\mathrm{air}})$ if the entire ice sheet temperature is implicitly set to T_{air} as it done in Pattyn et al. (2012). To overcome this issue and obtain enough grounding-line migration, we must span a wider yet realistic atmospheric temperature range (red line in Fig.4b).

Figure 5 illustrates the implications on the thermal state and the extent of the ice sheet under the air temperature forcing depicted in Fig. 4a. We note the temperature proximity to melting point at the base in all panels due to the combined contribution
395 of geothermal heatflux and frictional heat dissipation. Even so, most of the ice sheet temperature is determined by T_{air} and determines the overall extent through the viscosity.

We can still compare the grounding line position with the semi-analytical results in Schoof (2007) by converting the ice rate factor $A(T)$ to the corresponding temperature. Two remarks are worth noting here. First, the corresponding temperature values for the MISMIP forcing $A(T)$ are relatively high (always above -25ºC) compared to mean surface temperatures in
400 Greenland and Antarctica (Dee et al., 2011). Second, the ice-sheet region that best reproduces the semi-analytical solutions is the grounding line base (i.e., $x = L$, $n_z = 1$). In other words, for an active thermodynamics, the air temperature forcing must be strong enough to perturb the entire ice column down to the base so that the grounding line undergo migration. Otherwise, the insulating effect of the ice leaves the ice sheet base nearly unchanged with an equilibrium temperature strongly influenced by the geothermal heat flux (Moreno-Parada et al., 2022).

405 The warmest atmospheric boundary condition leads to a grounding line base near the melting point (Fig. 4d). As the air temperature is cooled down to -80ºC, this region also diminishes its temperatures, but with a notably reduced amplitude (Fig. 5). Unlike the ice surface, where the forcing temperature falls from -15ºC to -80ºC, the grounding line base reaches a minimum temperature of -23ºC (Fig. 4c).

In terms of the hysteresis behaviour, the jump over the retrograde region of the bed geometry occurs at a grounding line
410 basal temperature of -20ºC, far above the semi-analytical counterpart. On the contrary, as the system is forced with higher temperatures, the retreat takes place at neatly at the same temperature predicted by the boundary layer theory -18ºC.
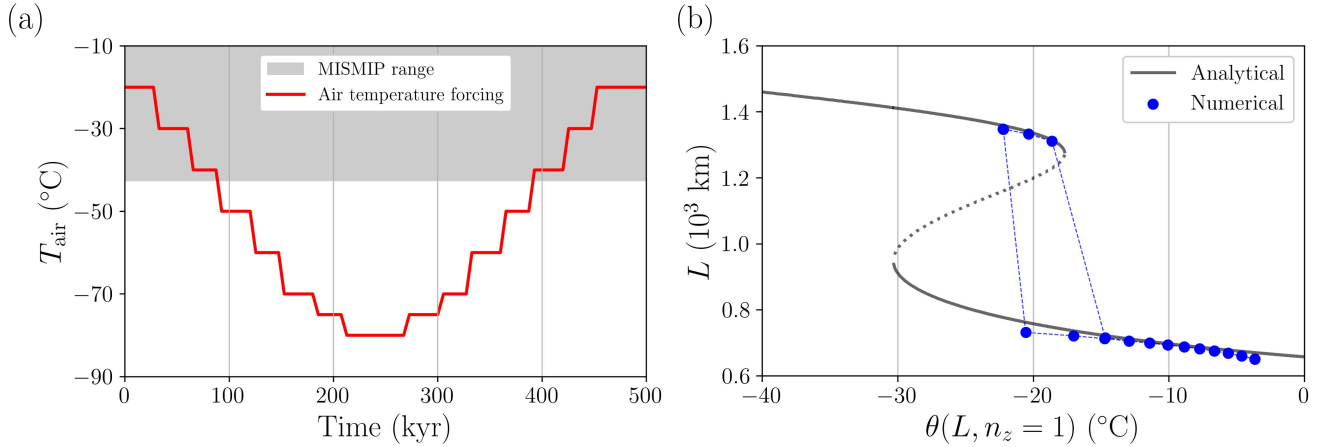
Figure 4. Overdeepened bed experiment. (a) Red solid line: Nix air temperature forcing $T_{air}(t)$, shaded grey: range spanned by MISMIP ice rate factor conversion to temperatures. (b) Grounding line position as a function of the grounding line ice temperature immediately above the base level $n_z = 1$. Semi-analytical results from Schoof (2007) are converted into temperatures by applying a simple Arrhenius law in the ice rate factor $A(T)$.

6.2.2 Ocean temperature anomalies ΔT_{oce} forcing

In this scenario, we apply ocean temperature anomalies with respect to a reference value T_0, so that $\Delta T_{oce} = T - T_0$. We then convert these temperature anomalies into sub-shelf melting at the grounding line (e.g., Favier et al., 2019) by computing any
415   of the parametrizations shown in Section 3.8.

We first perform two identical hysteresis experiments forced by ΔT_{oce} that solely differ on the thermodynamic treatment of the ice: an idealised fixed ice rate factor A (Fig 6, blue curve) and a more realistic active thermodynamic scenario with a constant boundary condition T_{air} (Fig 6, red curve). Results show that active thermodynamics narrows the width of the hysteresis loop. This behaviour resembles the one obtained for the atmospheric-forced simulations (Fig. 4), where we find a
420   clear narrowing of the hysteresis width compared to the semi-analytical solutions.

In addition to the experiments carried out to assess the importance of thermodynamics on the hysteresis behaviour of a marine terminating ice sheet, we have performed a sensitivity study to quantify the differences caused by parameter uncertainty (e.g., Favier et al., 2019), particularly on the heat exchange velocity γ.

Figure 7 illustrates the high sensitivity to that stems from the heat exchange velocity parameter γ. It is worth noting that the
425   retreat is much more sensitive to the particular γ choice than the later advance as the anomalies approach zero. Namely, all intermediate values advance at $\Delta T_{oce} = +1.5$ºC. On the contrary, the retreat occurs for a wider range of temperature anomalies from $+4.5$ºC to $+6.5$ºC for $\gamma = 2.1 \times 10^{-5}$ m/s and 1.3×10^{-5} m/s, respectively.

For a quadratic sub-shelf parametrisation (Eq. 22), the retreat takes place at $\Delta T_{oce} = +2.5$ºC for the highest heat exchange velocity calibrated in Favier et al. (2019), i.e., $\gamma = 100 \times 10^{-5}$ m/s. Even the lowest parameter value presented in the same
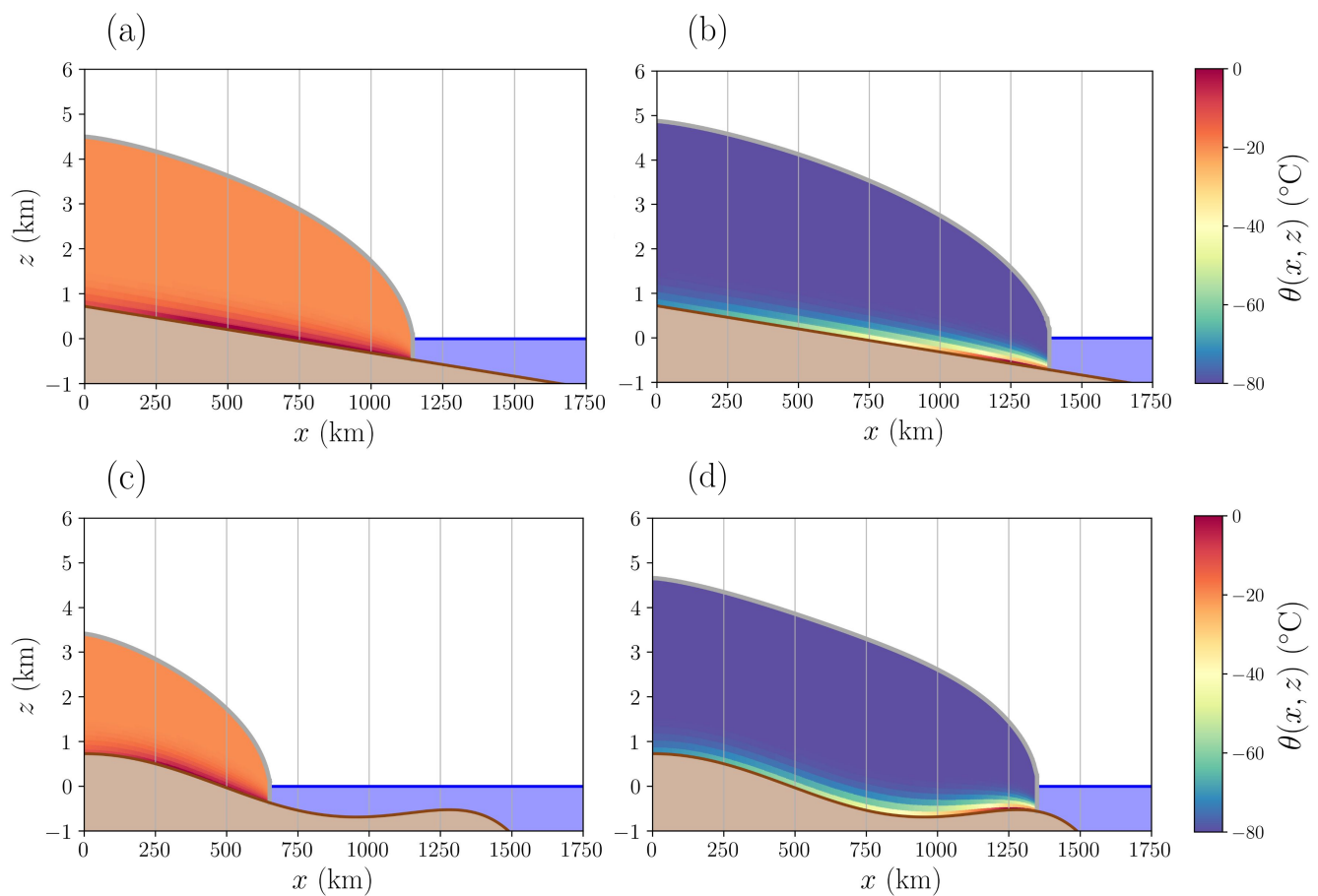
Figure 5. Ice sheet extent and temperature distribution for the prograde (a, c) and the overdeepened (b, d) bed geometries. Retreated (a, b) and advanced configurations (c, d) under the air temperature forcing in the thermodynamically active scenario (i.e., $A = f(T)$). Left column: $t = 30$ kyr. Right column: $t = 250$ kyr. Colours indicate the ice temperature at the given time.
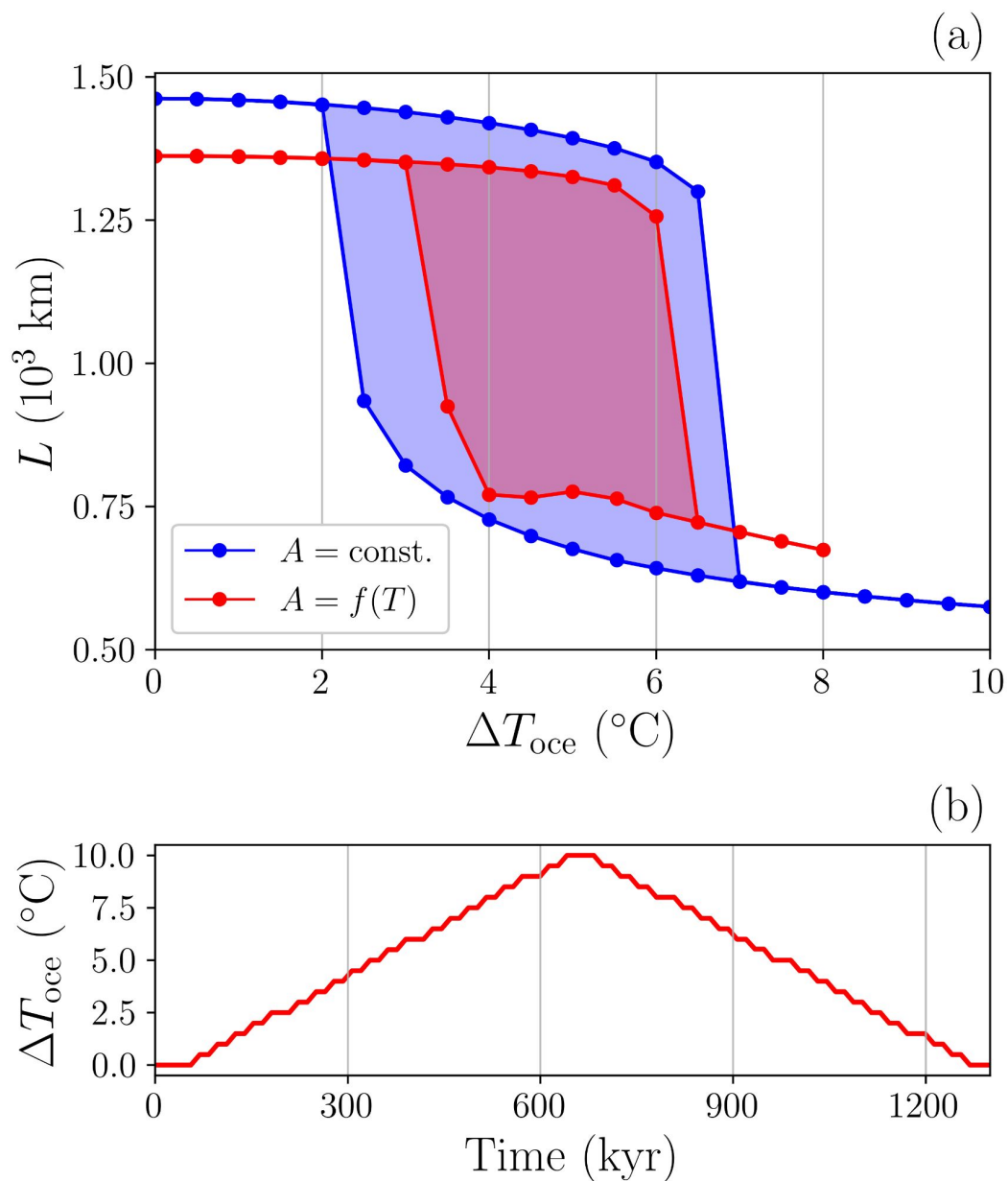
Figure 6. (a) Hysteresis experiments for the overdeepened bed geometry forced via slowly-varying ocean temperature anomalies $\Delta T_{\mathrm{oce}}(t)$. Blue: constant ice rate factor $A = 10^{-26}$ Pa^{3}s. Red: active thermodynamics $A = f(T)$ with fixed boundary condition $T_{\mathrm{air}} = -80$ ℃. Each forcing step is ran for 40 kyr to ensure quasi-equilibrium (solid dots). A quadratic sub-shelf parametrisation is employed in both scenarios. Heat exchange velocity parameter $\gamma = 5 \times 10^{-4}$ m/s. (b) External forcing time series: ocean temperature anomalies $\Delta T_{\mathrm{oce}}(t)$.
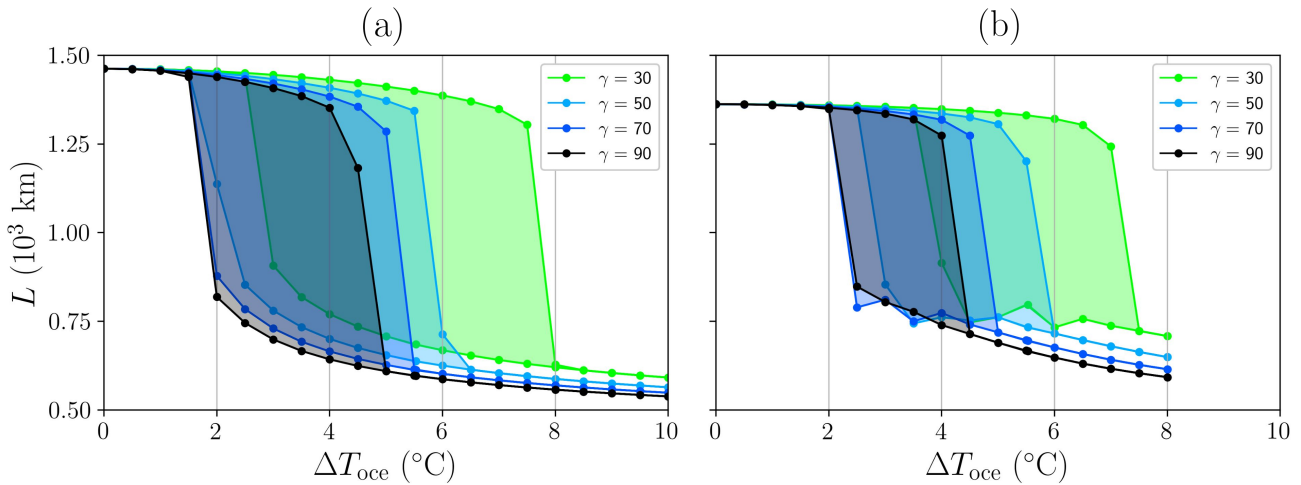
Figure 7. Sensitivity tests. As in Fig. 6a, but for (a) Constant ice rate factor $A = 10^{-26}$ Pa^{3}s. (b) Active thermodynamics with fixed T_{air}. Values of the heat exchange velocity parameter γ are given in 10^{-5} m/s and fall within the spanned range in Favier et al. (2019).

work also presents a retreat if the ocean temperature anomalies reach $\Delta T_{\mathrm{oce}} = +6.5$ºC. Multiple different values of γ advance back at nearly the same particular forcing value ΔT_{oce} 7, whereas the retreat happens at significantly different values. To illustrate this, we can take the hysteresis loops corresponding to $\gamma = 20 \times 10^{-5}$ m/s, 25×10^{-5} m/s, 35×10^{-5} m/s. They respectively retreat at $\Delta T_{\mathrm{oce}} = +5.5$ºC, $+5.0$ºC and $+4.5$ºC, whereas the advance take place at precisely the same anomaly value $\Delta T_{\mathrm{oce}} = +2.5$ºC.

7 Discussion

The results of our MISMIP benchmark experiments are successful given the good agreement between our numerical solution and the semi-analytical work of Schoof (2007) (Fig. 3). From a modeling perspective, our grounding line position is slightly shifted upstream, like in other moving grid models shown in Pattyn et al. (2012). Nevertheless, a sensitivity test to spatial resolution (not shown) shows an asymptotic convergence towards the semi-analytical solution, thus providing robustness to our results. A further comparison among Nix velocity solvers show an excellent agreement on the equilibrium solutions for both bed geometries herein studied: downward sloping and overdeepening.

For active thermodynamics and air temperature forcing, the corresponding temperature range spanned by MISMIP ice rate factor $A(T)$ does not yield a full advance/retreat of the ice sheet. This can be understood by the insulating effect of the ice sheet. The MISMIP idealised forcing with varying rate factor simultaneously modifies the ice viscosity over the entire domain, whereas the real temperatures given by an active thermomechanical solver will adjust to the new surface temperature (Fig. 4). This further means that the impact on the viscosity is weaker as there are other heat sources as the basal friction dissipation and the geothermal heat flow.

The stability of the system is accordingly perturbed, as shown in Fig. 6. Particularly, the bistability of the system is reduced, in the sense that a narrower range of perturbation values have two stable solutions. To illustrate this, for a rate factor $A = 10^{-26}$ Pa^{3}s, the oceanic anomaly perturbation ranges from $\Delta T_{\mathrm{oce}} = +1.5$ to $+6.5$ºC, whereas for the thermomechanically active scenario with constant T_{air}, the bistability solution is only found for smaller range from a $\Delta T_{\mathrm{oce}} = +3.0$ to $+6.0$ºC. This can be understood as the result of a thermal adjustment that occurs when the temperature of the ice can evolve in time. As the forcing changes over time (i.e., the ocean temperature anomalies), the ice flux at the grounding line is modified and the inland ice thickness is perturbed accordingly. The new ice thickness distribution implies a slightly different temperature solution and the viscosity is consequently modified. Knowing that the viscosity field determines the velocity solution via the stress balance, we therefore find a clear feedback that allows for the ice sheet to adjust if thermodynamics are active.

It is worth noting the fundamental role of vertical advection if the system is to be forced with air temperatures. Both the magnitude of vertical advection and its vertical dependency determine the temperature distrubution within the ice (Moreno-Parada et al., 2022). Setting the vertical advection at the surface equal to the accumulation (0.3 m/yr) is a standard choice and becomes necessary if a full advance/retreat is to be simulated. Otherwise, most of the ice interior remains too warm due to geothermal and frictional heat sources and the vertically-averaged viscosity remains too low for the grounding line to advance (not shown here).

We must also discuss the calibrated values of γ_T (Favier et al., 2019). The impact on the hysteresis behaviour is interesting as it does not imply a symmetric effect on the retreat/advance of the ice sheet (Fig. 7). Strictly speaking, the temperature anomaly necessary for the ice sheet to retreat is far more sensitive to the particular γ value than the anomaly necessary to advance. One potential explanation for this interesting behaviour rests on the very nature of the melting/calving parametrisation at the grounding line. Since M grows with ΔT_{oce} (Eq. 21 and 22), the difference among M values for a fixed γ increases with the temperature anomaly. Hence, knowing that the advance occurs when the ice flux value reaches a certain value at the grounding line, the temperature anomaly range covered by different γ that yield such a melting/calving values is smaller (as $\Delta T_{\mathrm{oce}} \rightarrow 0$).

8 Conclusions

We have presented and described the thermomechanically-coupled 2D model Nix. There are a number of novelties compared to other two-dimensional models: a stress balance given by the Blatter-Pattyn approximation, a fully coupled thermodynamics solver, explicit calculation of the grounding line by a stretched coordinate system, stochastic boundary conditions capability, adaptative time stepping and potential melting/calving at the grounding line. Nix model allows the user to choose between explicit and implicit solvers for the main differential equations, while numerical stability is ensured by a staggered grid.

First, we have tested Nix's performance by reproducing Experiments 1, 2 and 3 from MISMIP benchmarks (Pattyn et al., 2012). Results were further compared to semi-analytical solutions (Schoof, 2007) yielding an excellent agreement for all Stokes approximation available in Nix: SSA, DIVA and Blatter-Pattyn. In general, our grounding line position slightly understimates the boundary layer results in Schoof (2007), likewise all moving-grid models participating in MISMIP. The well-known hysteresis behaviour in Experiment 3 is also well captured.

We increase the complexity of the system described by solving the associated heat problem. This allows us to investigate to which extent the hysteresis behavior under parameter variations is perturbed. In so doing, we designed two different suites of experiments regarding the variable forcing of the system: air temperatures T_{air} and ocean temperature anomalies ΔT_{oce}.

485   When forcing with air temperatures, the hysteresis loop width is reduced as the dynamics are perturbed via the ice viscosity dependency on temperature. In an idealised overdeepened bed geometry, it is necessary to reach air temperatures below -70ºC for the grounding line to advance beyond the bedrock local maximum.

If the system is instead forced by ocean temperature anomalies (i.e., melting/calving at the grounding line), we find that the hysteresis behaviour persists. Notably, the ocean temperature anomaly at which the ice sheet retreats depends on the particular heat exchange parameter. Our results show that the quadratic parametrisation retreats at $\Delta T_{\mathrm{oce}} = +6.0$ºC of temperature

490   anomaly. The system advances back to its unperturbed state at $\Delta T_{\mathrm{oce}} = +3.0$ºC for the quadratic parametrisation.

More generally, irrespective of the particular external forcing applied (i.e., oceanic or atmospheric), a thermodynamically active ice sheet shows a narrowing hysteresis loop as a result of the internal feedback among ice temperature, stress balance and viscosity.

Author contributions. Daniel Moreno-Parada built the entire model, ran all the simulations, analysed the results and wrote the paper. All

495   other authors contributed to analyse the results and writing the paper.

Financial support. This research has been supported by the Spanish Ministry of Science and Innovation (project IceAge, grant no. PID2019-110714RA-100), the Ramón y Cajal Programme of the Spanish Ministry for Science, Innovation and Universities (grant no. RYC-2016-20587) and the European Commission, H2020 Research Infrastructures (TiPES, grant no. 820970).

Competing interests. The authors have no competing interests to declare.

500   *Code availability.* Nix ice-sheet model v1.0 is in a persistent Zenodo repository (Moreno-Parada et al., 2023): https://doi.org/10.5281/zenodo.10228874. Additionally, there is a GitHub repository where current and future versions of the software can be accessed at: https://github.com/d-morenop/nix

505

Appendix A: Discretization schemes

We herein elaborate on a thorough description of the discretization schemes of our flow line model where we follow the ordinary notation $q(\sigma_i, \zeta_j, \tau_n) \equiv q_{i,j}^n$.

510   The position in the spatial coordinates is then given by $\sigma_i = i\Delta\sigma_{i+1/2}$ and $\zeta_j = j\Delta\zeta_{j+1/2}$ and $\tau_n = n\Delta\tau$. The fractional index implies that the point $(i+1/2, j)$ lies between (i,j) and $(i+1,j)$ and analogously for the vertical index j. Note that Nix allows for a nonuniform spatial grid where the spacing between two consecutive points follows a desired distribution (polynomial or exponential). This yields high resolutions near the grounding line whilst minimising the total number of grid points. The horizontal index $i \in \mathcal{W}_r = \{0, 1, 2, ..., r\}$ where r is the number of points in which the horizontal axis is divided.

515   Likewise, the vertical index follows $j \in \mathcal{W}_p = \{0, 1, 2, ..., p\}$ where p is the number of vertical layers.

Appendix: A1: Blatter-Pattyn stress balance discretization.

The discretization is straightforward for an Arakawa-C grid. The position of the grounding line $L(t)$ is located on the velocity grid (following Vieli and Payne, 2005). Thus, if the horizontal axis is divided in r points, the ice thickness grid ranges $i = 0, 1, ..., r - 1$, whereas the velocity grid (staggered) indexes read $i = 1/2, \ 3/2, ..., r - 1/2$.

520   The Blatter-Pattyn stress balance can be written as:

$$\frac{2}{L^2 \Delta\sigma_{i+1/2}} \left[\eta_{i+1,j} \frac{u_{i+3/2,j} - u_{i+1/2,j}}{\Delta\sigma_{i+3/2} + \Delta\sigma_{i+1/2}} - \eta_{i,j} \frac{u_{i+1/2,j} - u_{i-1/2,j}}{\Delta\sigma_{i+1/2} + \Delta\sigma_{i-1/2}} \right] +$$

$$\frac{1}{2(H_i)^2 \Delta\zeta_{j+1/2}} \left[\eta_{i,j+1} \frac{u_{i,j+3/2} - u_{i,j+1/2}}{\Delta\zeta_{j+3/2} + \Delta\zeta_{j+1/2}} - \eta_{i,j} \frac{u_{i,j+1/2} - u_{i,j-1/2}}{\Delta\zeta_{j+1/2} + \Delta\zeta_{j-1/2}} \right] = \rho g \frac{h_{i+1} - h_i}{L \Delta\sigma_{i+1/2}}, \tag{A1}$$

We thus have a linear system of $6 \times r \times p$ unknowns that can be solved applying standard linear algebraic solvers. For each timestep, we build a matrix of coefficients with dimension $(rp) \times (rp)$:

$$\underset{(rp)\times(rp)}{A} * \underset{(rp)\times(1)}{u} = \underset{(rp)\times(1)}{F} \tag{A2}$$

525   Since our discretization stencil includes 6 points: $(i+3/2, j)$, $(i+1/2, j)$, $(i-1/2, j+1)$, $(i, j+3/2)$, $(i, j+1/2)$ and $(i, j-1/2)$, we obtain a sparse matrix that allows for optimised inversion. For $r = 500$ and $p = 25$, only a 0.048% of the coefficient matrix are nonzero entries:

$$\left(\begin{array}{ccccccccc} & & & & & & & & \\ & & & & & & & & \\ & & & & & & & & \\ \alpha_{i-2M,j} & \cdots & \alpha_{i-M,j} & \cdots & \alpha_{i,j-1/2} & \alpha_{i,j+1/2} & \cdots & \alpha_{i+M,j}\cdots & \alpha_{i+2M,j} \\ & & & & & & & & \\ & & & & & & & & \\ & & & & & & & & \\ & & & & & & & & \end{array}\right) \left(\begin{array}{c} u_{i-3/2,j} \\ \vdots \\ u_{i-1/2,j} \\ \vdots \\ u_{i,j-1/2} \\ u_{i,j+1/2} \\ \vdots \\ u_{i+1/2,j} \\ \vdots \\ u_{i+3/2,j} \end{array}\right) = \left(\begin{array}{c} F_{i-3/2,j} \\ \vdots \\ F_{i-1/2,j} \\ \vdots \\ F_{i,j-1/2} \\ F_{i,j+1/2} \\ \vdots \\ F_{i+1/2,j} \\ \vdots \\ F_{i+3/2,j} \end{array}\right) \tag{A3}$$

Appendix: A2: DIVA/SSA stress balance discretization.

The discretization is straightforward for a staggered grid. The position of the grounding line $L(t)$ is located on the staggered grid (following Vieli and Payne, 2005). Thus, if the domain is divided in n points, the ice thickness grid ranges $i = 0, 1, ..., r-1$, whereas the velocity grid (staggered) indexes read $i = 1/2, 3/2, ..., r-1/2$.

The SSA stress balance can be then written as (note that the factor 2 difference in Eq. B.15, Vieli and Payne, 2005 since their viscosity definition is not preceded by $1/2$ is cancelled by the average between two consecutive grid lengths $\Delta\sigma$ necessary to compute the velocity gradients):

$$\frac{2}{L^2\Delta\sigma_{i+1/2}}\left[\eta_{i+1}H_{i+1}\frac{u_{i+3/2,j}-u_{i+1/2,j}}{\Delta\sigma_{i+3/2}+\Delta\sigma_{i+1/2}} - \eta_i H_i\frac{u_{i+1/2,j}-u_{i-1/2,j}}{\Delta\sigma_{i+1/2}+\Delta\sigma_{i-1/2}}\right]$$
$$-\beta_{i+1/2}^2 u_{i+1/2} = \rho g\frac{H_{i+1}+H_i}{2}\frac{h_{i+1}-h_i}{L\Delta\sigma_{i+1/2}}, \tag{A4}$$

where the friction coefficient β^2 reads:

$$\beta_{i+1/2} = Cu_{i+1/2}^{m-1}, \tag{A5}$$

so that $\tau_b = \beta^2 u$.

Assuming our domain is divided in n points, the corresponding tridiagonal matrix is built at every time step as (where we have dropped the super-index to lighten the notation):

$$\left(\begin{array}{cccccc} B_0 & C_0 & & & & \\ A_1 & B_1 & C_1 & & & \\ & A_2 & B_2 & \ddots & & \\ & & \ddots & \ddots & C_{r-2} & \\ & & & A_{r-1} & B_{r-1} \end{array}\right) \left(\begin{array}{c} u_{1/2} \\ u_{3/2} \\ \vdots \\ u_{r-3/2} \\ u_{r-1/2} \end{array}\right) = \left(\begin{array}{c} F_0 \\ F_1 \\ \vdots \\ F_{r-2} \\ F_{r-1} \end{array}\right) \tag{A6}$$

where $A_0 = C_{n-1} = 0$ by definition.

The non-zero entries of the matrix and the inhomogeneous term read:

$$A_i = \gamma_i \eta_i H_i$$

$$B_i = -\gamma_i \left(\eta_{i+1} H_{i+1} + \eta_i H_i \right) - \beta_i^2$$

$$C_i = \gamma_i \eta_{i+1} H_{i+1}$$

$$F_i = \rho g \frac{H_{i+1} + H_i}{2} \frac{h_{i+1} - h_i}{L \Delta \sigma_{i+1/2}} \tag{A7}$$

where $\gamma_i = 2/(L \Delta \sigma_{i+1/2})^2$.

For the edge of the matrix (i.e., $i = n-1$), we use the following values:

$$A_{r-1} = \eta_{r-1} H_{r-1}$$

$$B_{r-1} = -\gamma_{r-1} \left(\eta_{r-1} H_{r-1} \right) - \beta_{n-1}^2$$

$$C_{r-1} = 0$$

$$F_{r-1} = \rho g H_{r-1} \frac{h_{r-1} - h_{r-2}}{L \Delta \sigma_{r-3/2}} \tag{A8}$$

For the boundary values, we set (note that, in the staggered grid, $u_{1/2}$ is the very first velocity value of the domain):

$$u_{1/2} = -u_{3/2},$$

$$u_{r-1/2} = u_{r-3/2} + \frac{L \Delta \sigma_{r-3/2}}{8 \eta_{r-1}} \left(\rho g H_{r-1}^2 - \rho_w g D^2 \right) \tag{A9}$$

where D is the bedrock depth below sea level, the first equality yields from symmetry arguments at the ice divide ($i = 1$) and the second implies that the ice momentum is equated by the hydrostatic pressure of the water.

Appendix: A2: Advection discretization

For the advection equation we also chose an implicit scheme for numerical stability:

$$\frac{H_i^{n+1} - H_i^n}{\Delta \tau^n} = \sigma_i \frac{\dot{L}^n}{L^n} \frac{H_{i+1}^{n+1} - H_{i-1}^{n+1}}{\left(\Delta \sigma_{i+1/2} + \Delta \sigma_{i-1/2} \right)} - \frac{2 \left(q_{i+1/2}^{n+1} - q_{i-1/2}^{n+1} \right)}{L^n \left(\Delta \sigma_{i+1/2} + \Delta \sigma_{i-1/2} \right)} + S_i^n, \tag{A10}$$

where the ice flux is defined as:

$$q_{i+1/2} = u_{i+1/2} \frac{H_{i+1} + H_i}{2} \tag{A11}$$

However, at the grounding line we use:

$$q_{r-1/2} = u_{r-1/2} H_{r-1} \tag{A12}$$

The advection equation can be rewritten as:

$$A_i H_{i-1}^{n+1} + B_i H_i^{n+1} + C_i H_{i+1}^{n+1} = F_i \tag{A13}$$

so that the corresponding matrix is also tridiagonal:

$$A_i = \gamma_i^n \left(\sigma_i \dot{L} - u_{i-1} \right)$$
$$B_i = 1 + \gamma_i^n \left(u_i - u_{i-1} \right)$$
$$C_i = \gamma_i^n \left(-\sigma_i \dot{L} + u_i \right)$$
$$F_i = H_i^n + \Delta\tau^n S_i^n \tag{A14}$$

where $\gamma_i^n = \Delta\tau^n/2 \left(\Delta\sigma_{i+1/2} + \Delta\sigma_{i-1/2} \right) L^n$.

As the ice divide is located at $i=1$ (note that we start counting at $i=0$), the boundary condition then reads:

$$H_0^n = H_2^n, \tag{A15}$$

since $\sigma = 1$ is a symmetry axis.

Appendix: A3: Grounding line scheme

The terminus position L (i.e., the grounding line) is not fixed in time. Direct discretization of Eq. 18 in terms of σ-coordinates leads to:

$$\dot{L}^n \equiv \frac{dL}{d\tau} = \frac{-L^n \Delta\sigma_{r-1/2} S_{r-1}^n + 2 \left(q_{r-1/2}^n - q_{r-3/2}^n \right) / \left(\Delta\sigma_{r-1/2} + \Delta\sigma_{r-3/2} \right)}{H_{r-1}^n - H_{r-2}^n + \varrho \left(b_{r-1}^n - b_{r-2}^n \right)}, \tag{A16}$$

Appendix: A4: Thermodynamics discretization scheme

Unlike previous discretizations, the temperature field $\theta(\sigma, \zeta, \tau)$ has an additional dependency on the vertical coordinate ζ that brings a higher degree of complexity (Eq. 24).

The energy balance (Eq. 28) is discretized using an upwind scheme with a forward Euler step and a centred difference for the spatial derivatives. The lengthy expression reads:

$$\rho c \left[\frac{\theta_{i,j}^{n+1} - \theta_{i,j}^n}{\Delta\tau^n} - \sigma_i \frac{\dot{L}^n}{L^n} \frac{\theta_{i+1,j}^n - \theta_{i-1,j}^n}{\Delta\sigma_{i+1/2} + \Delta\sigma_{i-1/2}} + \right.$$
$$\left. - \frac{\zeta_{i,j}}{H_i^n} \frac{H_i^{n+1} - H_i^{n-1}}{2\Delta\tau^n} \frac{\theta_{i,j+1}^n - \theta_{i,j-1}^n}{\Delta\zeta_{i,j+1/2} + \Delta\zeta_{i,j-1/2}} \right] = \frac{k}{(H_i^n)^2} \frac{\theta_{i,j+1}^n - 2\theta_{i,j}^n + \theta_{i,j-1}^n}{\left(\Delta\zeta_{i,j+1/2} + \Delta\zeta_{i,j-1/2} \right)^2} +$$
$$-\rho c \frac{u_i^n}{L^n} \left[\frac{\theta_{i+1,j}^n - \theta_{i-1,j}^n}{\Delta\sigma_{i+1/2} + \Delta\sigma_{i-1/2}} - \left(\frac{b_{i+1} - b_{i-1}}{\Delta\sigma_{i+1/2} + \Delta\sigma_{i-1/2}} + \zeta_{i,j} \frac{H_{i+1}^n - H_{i-1}^n}{\Delta\sigma_{i+1/2} + \Delta\sigma_{i-1/2}} \right) \frac{\theta_{i,j+1}^n - \theta_{i,j-1}^n}{H_i^n \left(\Delta\zeta_{i,j+1/2} + \Delta\zeta_{i,j-1/2} \right)} \right] + \Phi_i^n \tag{A17}$$

Appendix: A5: Adaptative time stepping

We take an adaptative timestepping approach to enhance the computational performance of the flowline model. Unlike the

580   proportional-integral (PI) methods, we exploit the fact that Picard's iteration already computes a metric to determine convergence. Thus, without additional calculations, we let the new timestep to evolve within a range set by the user $[\Delta t_{\min}, \Delta t_{\max}]$ with a quadratic dependency on the error:

$$\Delta \tilde{t} = \left(1 - \left(\frac{\min\left[\varepsilon(t), \phi_{\mathrm{pic}}\right]}{\phi_{\mathrm{pic}}} \right)^2 \right)(\Delta t_{\max} - \Delta t_{\min}) + \Delta t_{\min}, \tag{A18}$$

where ϕ_{pic} is the tolerance on Picard's iteration and $\varepsilon(t)$ is the error on the current iteration defined as $\varepsilon^i = ||u^i - u^{i-1}||$ (De

585   Schmedt et al., 2010). If the solution has not converged in the given timestep (i.e., $\varepsilon > \phi_{\mathrm{pic}}$), Eq. Equation **??** ensures that the timestep is set to the minimum value.

Then, we apply some relaxation to provide stability and avoid spurious oscillations:

$$\Delta t = \alpha \Delta t + (1 - \alpha)\Delta \tilde{t}, \tag{A19}$$

where $\alpha = 0.7$. And we finally ensure that the timestep is no greater than the CFL condition:

590   $$\Delta t = \min\left[\Delta t, \Delta t_{\mathrm{CFL}}\right] \tag{A20}$$

Appendix B: Stochastic boundary conditions

Internal climatic variability arises from chaotic fluctuation and its he effect over a real ice sheet mostly comes from the atmosphere and the ocean. The latter two interact with an ice sheet via the surface mass balance and the frontal melting/calving at the grounding line. We then need to create two random time series that fulfil three conditions: (1) random nature, (2) correlated

595   with each other and (3) have a prescribed persistence.

We now describe a Fourier transform method to create such a series following Christian et al. (2022). Nevertheless, the methods herein presented is completely general and can generate random time series of any variables provided that the system is described by a first-order autoregressive process.

We simply start with the power spectrum of an AR-1 process as a function of the frequency:

600   $$P(\nu) = \frac{P_0}{1 + r^2 - 2r\cos(2\pi\nu\Delta t)} \tag{B1}$$

where P_0 scales the total variance (here we employ $P_0 = 1$), r is the autocorrelation coefficient at a lag Δt.

The persistence time τ_{AR1} (i.e., decorrelation time) then reads:

$$\tau_{\mathrm{AR1}} = \frac{\Delta t}{1 - r} \tag{B2}$$

and we can simply obtain a random complex spectrum from a random phase rotation and then applying the inverse Fourier

605   transform:

$$P(t) = \mathcal{F}^{-1}\left[P(\nu)e^{i\phi} \right] \tag{B3}$$

where $\phi \in [0, 2\pi]$.

610

Financial support. This research is TiPES contribution no. XXX and has been supported by the European Union Horizon 2020 research and innovation programme (grant no. 820970), the Ramón y Cajal Programme of the Spanish Ministry for Science, Innovation and Universities (grant no. RYC-2016-20587). Alexander Robinson received funding from the European Union (ERC, FORCLIMA, 101044247).

References

615 Alley, R. B., Blankenship, D. D., Bentley, C. R., and Rooney, S. T.: Deformation of till beneath ice stream B, West Antarctica, Nature, 322, 57–59, https://doi.org/10.1038/322057a0, 1986.

Arakawa, A. and Lamb, V. R.: Computational Design of the Basic Dynamical Processes of the UCLA General Circulation Model, in: Methods in Computational Physics: Advances in Research and Applications, pp. 173–265, Elsevier, https://doi.org/10.1016/b978-0-12-460817-7.50009-4, 1977.

620 Arthern, R. J. and Williams, C. R.: The sensitivity of West Antarctica to the submarine melting feedback, Geophysical Research Letters, 44, 2352–2359, https://doi.org/10.1002/2017gl072514, 2017.

Arthern, R. J., Hindmarsh, R. C. A., and Williams, C. R.: Flow speed within the Antarctic ice sheet and its controls inferred from satellite observations, Journal of Geophysical Research: Earth Surface, 120, 1171–1188, https://doi.org/10.1002/2014jf003239, 2015.

Asay-Davis, X. S., Jourdain, N. C., and Nakayama, Y.: Developments in Simulating and Parameterizing Interactions Between the Southern
625 Ocean and the Antarctic Ice Sheet, Current Climate Change Reports, 3, 316–329, https://doi.org/10.1007/s40641-017-0071-0, 2017.

Aschwanden, A., Aðalgeirsdóttir, G., and Khroulev, C.: Hindcasting to measure ice sheet model sensitivity to initial states, The Cryosphere, 7, 1083–1093, https://doi.org/10.5194/tc-7-1083-2013, 2013.

Bamber, J. L., Vaughan, D. G., and Joughin, I.: Widespread Complex Flow in the Interior of the Antarctic Ice Sheet, Science, 287, 1248–1250, https://doi.org/10.1126/science.287.5456.1248, 2000.

630 Bentley, C. R.: Rapid sea-level rise from a West Antarctic ice-sheet collapse: a short-term perspective, Journal of Glaciology, 44, 157–163, https://doi.org/10.3189/s0022143000002446, 1998.

Blankenship, D. D., Bentley, C. R., Rooney, S. T., and Alley, R. B.: Seismic measurements reveal a saturated porous layer beneath an active Antarctic ice stream, Nature, 322, 54–57, https://doi.org/10.1038/322054a0, 1986.

Blatter, H.: Velocity and stress fields in grounded glaciers: a simple algorithm for including deviatoric stress gradients, Journal of Glaciology,
635 41, 333–344, https://doi.org/10.3189/s002214300001621x, 1995.

Bueler, E. and Brown, J.: Shallow shelf approximation as a 'sliding law'in a thermomechanically coupled ice sheet model, J. Geophys. Res, 114, F03 008, 2009.

Christian, J. E., Robel, A. A., and Catania, G.: A probabilistic framework for quantifying the role of anthropogenic climate change in marine-terminating glacier retreats, The Cryosphere, 16, 2725–2743, https://doi.org/10.5194/tc-16-2725-2022, 2022.

640 Dee, D. P., Uppala, S. M., Simmons, A. J., Berrisford, P., Poli, P., Kobayashi, S., Andrae, U., Balmaseda, M. A., Balsamo, G., Bauer, P., Bechtold, P., Beljaars, A. C. M., van de Berg, L., Bidlot, J., Bormann, N., Delsol, C., Dragani, R., Fuentes, M., Geer, A. J., Haimberger, L., Healy, S. B., Hersbach, H., Hólm, E. V., Isaksen, L., Kållberg, P., Köhler, M., Matricardi, M., McNally, A. P., Monge-Sanz, B. M., Morcrette, J.-J., Park, B.-K., Peubey, C., de Rosnay, P., Tavolato, C., Thépaut, J.-N., and Vitart, F.: The ERA-Interim reanalysis: configuration and performance of the data assimilation system, Quarterly Journal of the Royal Meteorological Society, 137, 553–597,
645 https://doi.org/10.1002/qj.828, 2011.

Dukowicz, J. K., Price, S. F., and Lipscomb, W. H.: Consistent approximations and boundary conditions for ice-sheet dynamics from a principle of least action, Journal of Glaciology, 56, 480–496, https://doi.org/10.3189/002214310792447851, 2010.

Engelhardt, H., Humphrey, N., Kamb, B., and Fahnestock, M.: Physical Conditions at the Base of a Fast Moving Antarctic Ice Stream, Science, 248, 57–59, https://doi.org/10.1126/science.248.4951.57, 1990.

650 Favier, L., Jourdain, N. C., Jenkins, A., Merino, N., Durand, G., Gagliardini, O., Gillet-Chaulet, F., and Mathiot, P.: Assessment of sub-shelf melting parameterisations using the ocean–ice-sheet coupled model NEMO(v3.6)–Elmer/Ice(v8.3), Geoscientific Model Development, 12, 2255–2283, https://doi.org/10.5194/gmd-12-2255-2019, 2019.

Fretwell, P., Pritchard, H. D., Vaughan, D. G., Bamber, J. L., Barrand, N. E., Bell, R., Bianchi, C., Bingham, R. G., Blankenship, D. D., Casassa, G., Catania, G., Callens, D., Conway, H., Cook, A. J., Corr, H. F. J., Damaske, D., Damm, V., Ferraccioli, F., Forsberg, R., Fujita,

655 S., Gim, Y., Gogineni, P., Griggs, J. A., Hindmarsh, R. C. A., Holmlund, P., Holt, J. W., Jacobel, R. W., Jenkins, A., Jokat, W., Jordan, T., King, E. C., Kohler, J., Krabill, W., Riger-Kusk, M., Langley, K. A., Leitchenkov, G., Leuschen, C., Luyendyk, B. P., Matsuoka, K., Mouginot, J., Nitsche, F. O., Nogi, Y., Nost, O. A., Popov, S. V., Rignot, E., Rippin, D. M., Rivera, A., Roberts, J., Ross, N., Siegert, M. J., Smith, A. M., Steinhage, D., Studinger, M., Sun, B., Tinto, B. K., Welch, B. C., Wilson, D., Young, D. A., Xiangbin, C., and Zirizzotti, A.: Bedmap2: improved ice bed, surface and thickness datasets for Antarctica, The Cryosphere, 7, 375–393, https://doi.org/10.5194/tc-7-

660 375-2013, 2013.

Goldberg, D. N.: A variationally derived, depth-integrated approximation to a higher-order glaciological flow model, Journal of Glaciology, 57, 157–170, https://doi.org/10.3189/002214311795306763, 2011.

Greve, R. and Blatter, H.: Dynamics of Ice Sheets and Glaciers, Springer Berlin Heidelberg, https://doi.org/10.1007/978-3-642-03415-2, 2009.

665 Grosfeld, K., Gerdes, R., and Determann, J.: Thermohaline circulation and interaction between ice shelf cavities and the adjacent open ocean, Journal of Geophysical Research: Oceans, 102, 15 595–15 610, https://doi.org/10.1029/97jc00891, 1997.

Hindmarsh, R. C.: The role of membrane-like stresses in determining the stability and sensitivity of the Antarctic ice sheets: back pressure and grounding line motion, Philosophical Transactions of the Royal Society A: Mathematical, Physical and Engineering Sciences, 364, 1733–1767, https://doi.org/10.1098/rsta.2006.1797, 2006.

670 Hindmarsh, R. C. A.: Qualitative Dynamics of Marine Ice Sheets, in: Ice in the Climate System, pp. 67–99, Springer Berlin Heidelberg, https://doi.org/10.1007/978-3-642-85016-5_5, 1993.

Hindmarsh, R. C. A.: Stability of ice rises and uncoupled marine ice sheets, Annals of Glaciology, 23, 105–115, https://doi.org/10.3189/s0260305500013318, 1996.

Joughin, I., MacAyeal, D. R., and Tulaczyk, S.: Basal shear stress of the Ross ice streams from control method inversions, Journal of

675 Geophysical Research: Solid Earth, 109, n/a–n/a, https://doi.org/10.1029/2003jb002960, 2004.

Joughin, I., Smith, B. E., and Schoof, C. G.: Regularized Coulomb Friction Laws for Ice Sheet Sliding: Application to Pine Island Glacier, Antarctica, Geophysical Research Letters, 46, 4764–4771, https://doi.org/10.1029/2019gl082526, 2019.

Lipscomb, W. H., Price, S. F., Hoffman, M. J., Leguy, G. R., Bennett, A. R., Bradley, S. L., Evans, K. J., Fyke, J. G., Kennedy, J. H., Perego, M., Ranken, D. M., Sacks, W. J., Salinger, A. G., Vargo, L. J., and Worley, P. H.: Description and evaluation of the Community Ice Sheet

680 Model (CISM) v2.1, Geoscientific Model Development, 12, 387–424, https://doi.org/10.5194/gmd-12-387-2019, 2019.

Ma, Y., Gagliardini, O., Ritz, C., Gillet-Chaulet, F., Durand, G., and Montagnat, M.: Enhancement factors for grounded ice and ice shelves inferred from an anisotropic ice-flow model, Journal of Glaciology, 56, 805–812, https://doi.org/10.3189/002214310794457209, 2010.

MacAyeal, D. R. and Barcilon, V.: Ice-shelf Response to Ice-stream Discharge Fluctuations: I. Unconfined Ice Tongues, Journal of Glaciology, 34, 121–127, https://doi.org/10.3189/s002214300000914x, 1988.

685 Minchew, B. M., Meyer, C. R., Robel, A. A., Gudmundsson, G. H., and Simons, M.: Processes controlling the downstream evolution of ice rheology in glacier shear margins: case study on Rutford Ice Stream, West Antarctica, Journal of Glaciology, 64, 583–594, https://doi.org/10.1017/jog.2018.47, 2018.

Moreno-Parada, D., Robinson, A., Montoya, M., and Alvarez-Solas, J.: On the periodicity of free oscillations for a finite ice column, https://doi.org/10.5194/tc-2022-97, 2022.

690   Moreno-Parada, D., Robinson, A., Montoya, M., and Alvarez-Solas, J.: Nix ice sheet model v1.0.0, https://doi.org/10.5281/ZENODO.10228874, 2023.

Nowicki, S. and Wingham, D.: Conditions for a steady ice sheet–ice shelf junction, Earth and Planetary Science Letters, 265, 246–255, https://doi.org/10.1016/j.epsl.2007.10.018, 2008.

Pattyn, F.: A new three-dimensional higher-order thermomechanical ice sheet model: Basic sensitivity, ice stream development, and ice flow

695   across subglacial lakes, Journal of Geophysical Research, 108, https://doi.org/10.1029/2002jb002329, 2003.

Pattyn, F. and Morlighem, M.: The uncertain future of the Antarctic Ice Sheet, Science, 367, 1331–1335, https://doi.org/10.1126/science.aaz5487, 2020.

Pattyn, F., Huyghe, A., Brabander, S. D., and Smedt, B. D.: Role of transition zones in marine ice sheet dynamics, Journal of Geophysical Research, 111, https://doi.org/10.1029/2005jf000394, 2006.

700   Pattyn, F., Schoof, C., Perichon, L., Hindmarsh, R. C. A., Bueler, E., de Fleurian, B., Durand, G., Gagliardini, O., Gladstone, R., Goldberg, D., Gudmundsson, G. H., Huybrechts, P., Lee, V., Nick, F. M., Payne, A. J., Pollard, D., Rybak, O., Saito, F., and Vieli, A.: Results of the Marine Ice Sheet Model Intercomparison Project, MISMIP, The Cryosphere, 6, 573–588, https://doi.org/10.5194/tc-6-573-2012, 2012.

Quiquet, A., Dumas, C., Ritz, C., Peyaud, V., and Roche, D. M.: The GRISLI ice sheet model (version 2.0): calibration and validation for multi-millennial changes of the Antarctic ice sheet, Geoscientific Model Development, 11, 5003–5025, https://doi.org/10.5194/gmd-11-

705   5003-2018, 2018.

Rignot, E., Mouginot, J., Scheuchl, B., van den Broeke, M., van Wessem, M. J., and Morlighem, M.: Four decades of Antarctic Ice Sheet mass balance from 1979–2017, Proceedings of the National Academy of Sciences, 116, 1095–1103, https://doi.org/10.1073/pnas.1812883116, 2019.

Robel, A. A., DeGiuli, E., Schoof, C., and Tziperman, E.: Dynamics of ice stream temporal variability: Modes, scales, and hysteresis, Journal

710   of Geophysical Research: Earth Surface, 118, 925–936, https://doi.org/10.1002/jgrf.20072, 2013.

Robel, A. A., Seroussi, H., and Roe, G. H.: Marine ice sheet instability amplifies and skews uncertainty in projections of future sea-level rise, Proceedings of the National Academy of Sciences, 116, 14 887–14 892, https://doi.org/10.1073/pnas.1904822116, 2019.

Robinson, A., Goldberg, D., and Lipscomb, W. H.: A comparison of the stability and performance of depth-integrated ice-dynamics solvers, The Cryosphere, 16, 689–709, https://doi.org/10.5194/tc-16-689-2022, 2022.

715   Schoof, C.: The effect of cavitation on glacier sliding, Proceedings of the Royal Society A: Mathematical, Physical and Engineering Sciences, 461, 609–627, https://doi.org/10.1098/rspa.2004.1350, 2005.

Schoof, C.: A variational approach to ice stream flow, Journal of Fluid Mechanics, 556, 227, https://doi.org/10.1017/s0022112006009591, 2006a.

Schoof, C.: Variational methods for glacier flow over plastic till, Journal of Fluid Mechanics, 555, 299,

720   https://doi.org/10.1017/s0022112006009104, 2006b.

Schoof, C.: Ice sheet grounding line dynamics: Steady states, stability, and hysteresis, J. Geophys. Res, 112, 2007.

Schoof, C.: Ice-sheet acceleration driven by melt supply variability, Nature, 468, 803–806, https://doi.org/10.1038/nature09618, 2010.

Schoof, C.: Marine ice sheet dynamics. Part 2. A Stokes flow contact problem, Journal of Fluid Mechanics, 679, 122–155, https://doi.org/10.1017/jfm.2011.129, 2011.

725 Schoof, C. and Hindmarsh, R. C. A.: Thin-Film Flows with Wall Slip: An Asymptotic Analysis of Higher Order Glacier Flow Models, The Quarterly Journal of Mechanics and Applied Mathematics, 63, 73–114, https://doi.org/10.1093/qjmam/hbp025, 2010.

Sergienko, O. V., Goldberg, D. N., and Little, C. M.: Alternative ice shelf equilibria determined by ocean environment, Journal of Geophysical Research: Earth Surface, 118, 970–981, https://doi.org/10.1002/jgrf.20054, 2013.

Shepherd, A. and Wingham, D.: Recent Sea-Level Contributions of the Antarctic and Greenland Ice Sheets, Science, 315, 1529–1532,
730 https://doi.org/10.1126/science.1136776, 2007.

Shepherd, A., Fricker, H. A., and Farrell, S. L.: Trends and connections across the Antarctic cryosphere, Nature, 558, 223–232, https://doi.org/10.1038/s41586-018-0171-6, 2018.

Stearns, L. A. and van der Veen, C. J.: Friction at the bed does not control fast glacier flow, Science, 361, 273–277, https://doi.org/10.1126/science.aat2217, 2018.

735 Teschl, G.: Ordinary Differential Equations and Dynamical Systems, Graduate studies in mathematics, American Mathematical Society, https://books.google.es/books?id=FZ0CAQAAQBAJ, 2012.

Thomas, R. H. and Bentley, C. R.: A Model for Holocene Retreat of the West Antarctic Ice Sheet, Quaternary Research, 10, 150–170, https://doi.org/10.1016/0033-5894(78)90098-4, 1978.

Truffer, M. and Fahnestock, M.: Rethinking Ice Sheet Time Scales, Science, 315, 1508–1510, https://doi.org/10.1126/science.1140469, 2007.

740 Tulaczyk, S.: Ice sliding over weak, fine-grained tills: Dependence of ice-till interactions on till granulometry, in: Glacial Processes Past and Present, Geological Society of America, https://doi.org/10.1130/0-8137-2337-x.159, 1999.

Tulaczyk, S., Kamb, B., Scherer, R. P., and Engelhardt, H. F.: Sedimentary processes at the base of a West Antarctic ice stream constraints from textural and compositional properties of subglacial debris, Journal of Sedimentary Research, 68, 487–496, https://doi.org/10.2110/jsr.68.487, 1998.

745 Vaughan, D. G. and Arthern, R.: Why Is It Hard to Predict the Future of Ice Sheets?, Science, 315, 1503–1504, https://doi.org/10.1126/science.1141111, 2007.

Veen, C. V. D. and Whillans, I.: Force Budget: I. Theory and Numerical Methods, Journal of Glaciology, 35, 53–60, https://doi.org/10.3189/002214389793701581, 1989.

Vieli, A. and Payne, A. J.: Assessing the ability of numerical ice sheet models to simulate grounding line migration, Journal of Geophysical
750 Research, 110, https://doi.org/10.1029/2004jf000202, 2005.

Weertman, J.: On the Sliding of Glaciers, Journal of Glaciology, 3, 33–38, https://doi.org/10.3189/s0022143000024709, 1957.

Weertman, J.: Stability of the Junction of an Ice Sheet and an Ice Shelf, Journal of Glaciology, 13, 3–11, https://doi.org/10.3189/s0022143000023327, 1974.

Whillans, I. M. and van der Veen, C. J.: The role of lateral drag in the dynamics of Ice Stream B, Antarctica, Journal of Glaciology, 43,
755 231–237, https://doi.org/10.3189/s0022143000003178, 1997.

Zoet, L. K. and Iverson, N. R.: A slip law for glaciers on deformable beds, Science, 368, 76–78, https://doi.org/10.1126/science.aaz1183, 2020.